ACOUSTIC TAGS FOR HIGH FREQUENCY SIDE-SCAN SONAR

A Thesis
Presented to
The Academic Faculty

by

Prakhar Srivastava

In Partial Fulfillment
of the Requirements for the Degree
Master of Science in Mechanical Engineering

Georgia Institute of Technology
May 2016

ACOUSTIC TAGS FOR HIGH FEQUENCY SIDE-SCAN SONAR

Approved by:

Dr. Karim Sabra, Advisor
School of Mechanical Engineering
Georgia Institute of Technology

Dr. Michael Leamy
School of Mechanical Engineering
Georgia Institute of Technology

Dr. Francois Guillot
School of Mechanical Engineering
Georgia Institute of Technology

Date Approved: 15 April 2016

ACKNOWLEDGEMENTS

Firstly, I would like to express gratitude to my advisor Dr. Karim Sabra for his valuable guidance, useful inputs and dedication to this work. I would also like to acknowledge the helpful contributions and feedbacks from Brendan Nichols throughout the learning process of this thesis project.

Lastly, I would like to thank Jueseok Kim, Avery Riddle, Amreeta Duttchoudhury, Aditi Kumar (in the undergraduate SONAR research team) for their timely help in setting up and carrying out the water tank experiments.

TABLE OF CONTENTS

LIST OF FIGURES

Page

SUMMARY

Autonomous underwater vehicles (AUVs) are used by several commercial, research, and military agencies for various applications. To facilitate the navigation of these underwater vehicles, tags and transponders are often used to mark underwater targets or tracks of interest. However, most underwater tag identification systems rely on an active source system and electronic hardware to broadcast a beacon acoustic signal. Such systems require extensive calibration at setup and are prone to high maintenance costs. This thesis work develops lower-cost, totally passive acoustic tags ("AcoustiCode") that are able to encode information which can be read by a conventional high-frequency side-scan SONAR. The AcoustiCode tags utilize Braggs scattering principle to create a unique reflected beampattern (an acoustic signature) that can be detected by a SONAR. The information is encoded in the unique spatial beampattern of each AcoustiCode tag. Numerical simulations and experimental testing in a water tank are conducted to investigate the performance of the proposed approach.

CHAPTER I

INTRODUCTION

Unmanned and autonomous underwater vehicles (UUVs, AUVs) are used by several commercial, research, and military agencies for various applications. Carrying out tasks such as studying ocean floors, military surveillance, tracking marine mammals, surveying/automated maintenance of oil pipelines, etc., requires the underwater vehicle to accurately locate and mark particular underwater targets or tracks of interest in order to navigate to the desired environment.

Navigation and positioning of underwater vehicles poses certain challenges since conventional above-ground methods are ineffective. Radio waves do not propagate well underwater [1], and electro-magnetic (EM) communication in seawater is characterized by high attenuation [2]. Hence, acoustic methods such as Sound Navigation and Ranging (SONAR) are often used for underwater communication links.

Acoustic transponders are generally used as "beacons" to guide the motion of a AUV; two types of acoustic positioning systems are primarily used [3]: long baseline (LBL), and ultra-short baseline (USBL). These methods are often used in combination [4] and utilize external transducer arrays and/or multiple transceivers to aid navigation. While LBL systems operating at 300kHz can provide location accuracy to within a few centimeters [3], they can be expensive and complex to deploy since multiple transponders have to be installed. Furthermore, these systems require extensive calibration at setup, and the

transducers have to be retrieved afterwards [4]. A simpler, cheaper system is desired for an underwater vehicle trying to locate and follow a stationary target or track of interest.

The objective of this work is to develop cost-effective, passive acoustic tags that can encode navigation information to an underwater vehicle. AcoustiCode tags consist of plates designed with an array of equally spaced grooves; the periodic surface structure utilizes Bragg scattering principle to create a unique reflected beampattern given an incident SONAR beam. Through both simulations and underwater tank testing, the performance of these tags is evaluated for various tag types. The feasibility of a SONAR position tracking system, and an underwater information encoding system using AcoustiCode tags is investigated.

CHAPTER II

BACKGROUND

2.1 Tracking Underwater Targets

The use of acoustics for underwater communication dates back to the second World War, when the underwater telephone was developed in 1945 in the United States for communicating with submarines [5]. It used a single side-band suppressed carrier modulation in the 8-11 kHz band with a range of a few kilometers. Since then, significant advancements have been made in the development of underwater acoustic communication systems in terms of their operational range and data transmitted. Acoustically controlled robots are used in various off-shore and deep sea applications, underwater data telemetry over 200 kilometers of horizontal distance has been achieved [6], and underwater networks are being established to support the Internet of Underwater Things [7].

Underwater applications often involve tracking information that is relayed from some source to a receiver. Traditionally, acoustic tags have been used to locate and track various underwater objects. Marine animal studies are often conducted with the help of acoustic transponders that are tagged to the fishes and tracked by SONAR [8]. In a typical responder location system, the base station transmits a request signal encoded with the identifier of a particular tag. The corresponding tag responds a signal that may be encoded with data indicating a status of the tag, or any other information [9]. The location of the tag can be

determined based on the time taken to receive the signal, and the beamforming direction measured by the hydrophone array.

While the transducers have become smaller and cheaper to produce since they were first introduced, large-scale implementation can be tedious due to the maintenance, cost, and initial calibration requirements of the electronic tag system. New, passive and non-electronic tag methods are being explored for an underwater robot carrying out surveillance tasks. The ARTag marker system [10] utilizes chromatic targets to carry out visual servoing of the AUV. The robot detects the pre-specified colored target markers. The ARTag marker uses a two-dimensional image, similar to the QR code [26], to encode information visually. The robot uses machine vision to scan the markers; this visual communication with the robot is used to affect changes in its movement/behavior. However, the ARTag marker system is limited by the visual range underwater; the robot can track the target in image-space only up to a maximum distance of two meters. To increase the range capability of such type of a passive tag system, a new version of the information coding marker system is desired that can utilize underwater acoustic communication instead.

The primary limitation of EM wave propagation in water is the high attenuation (specifically in seawater) due to the conductivity of water [2]. Hence, the use of acoustic tags permits a longer usability range. Furthermore, utilizing passive acoustic tags (as compared to using active acoustic beacons) will lower setup and maintenance costs, and reduce calibration complexity of the system.

2.2   Side-Scan SONAR

SONAR constitutes a vital part of every underwater navigation system. AUVs and Remotely Operated Underwater Vehicles (ROVs), along with submarines and other ships, are usually equipped with SONAR to sense the surroundings. SONAR works to remotely detect and locate objects underwater by emitting sound pulses and then recording their reflections. Range to an object can be obtained using the time delay between the outgoing and the echo pulses.

Side-scan SONAR consists of transducers mounted on either side of the SONAR (i.e. at both port side, starboard side). Figure 1a shows an example of a widely used commercial SONAR device. Side-scan SONARs are primarily designed to provide acoustic images of the seafloor [11]; however they are also useful tools for target detection, e.g. ship wrecks, pipelines and cables. Figure 1b shows an image result obtained from a typical side-scan SONAR [12]. Higher intensities of data in Figure 1b suggest more reflective surfaces such as shipwreck, bed rocks, metal, etc.

The acoustic beam in a side-scan SONAR propagates out on either side of the side-scan SONAR as shown in Figure 1c; in a typical side-scan SONAR, the beam is narrow in the horizontal plane (only 1-2°) and broad in the vertical plane (about 60° with a 20° main lobe) [13]. The narrow beamwidth provides sharp acoustic images, and helps rejecting noise from extraneous sources. Considering these advantages and the wide commercial use of side-scan SONARs, they are ideal for use in this study for development of AcoustiCode tags.

(a)   (b)

(c)
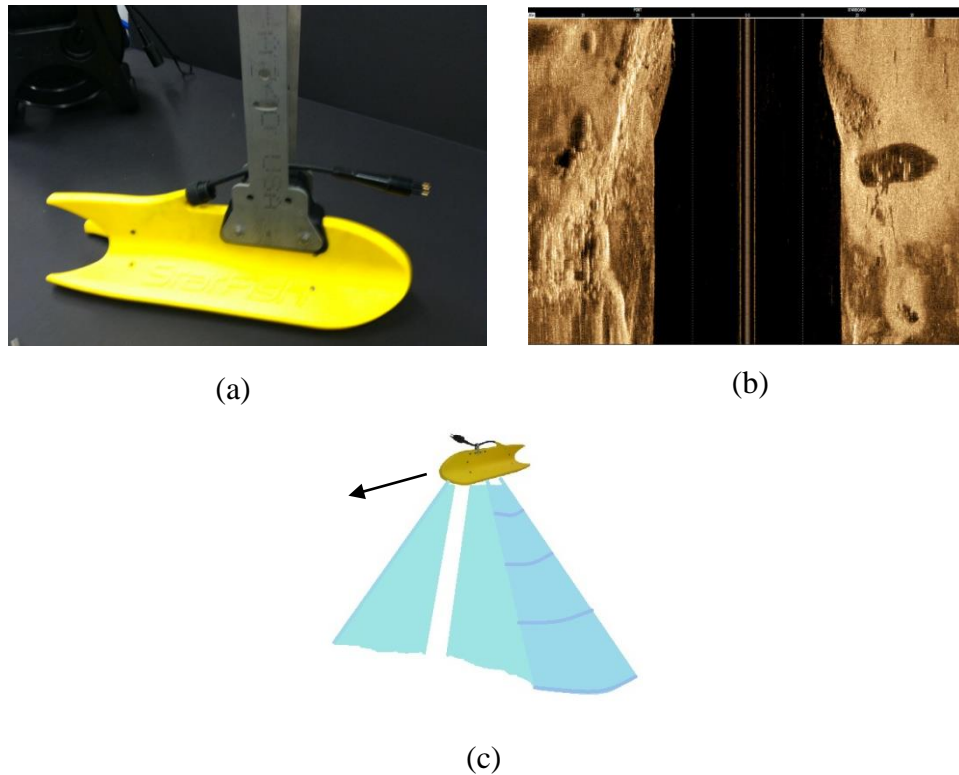
Figure 1: a) Tritech StarFish 452F, b) A shipwreck image captured by Starfish 452F [12], c) Schematic showing a typical narrow beam transmitted from the side-scan SONAR [27]

Commercially available high frequency side-scan SONARs can typically have a spatial resolution to within 3-5mm and their range of operation can vary from 50-200m [14]. While the resolution increases with higher frequencies, the range of operation decreases. The Tritech StarFish 452F shown in Figure 1a is used in this study. It sends out a chirp signal from 430-470kHz and has an operating range of upto 100m on each channel [27].

2.3 Ultrasonic Backscattering from Periodic Surfaces

The study of wave scattering on periodic surfaces has captured the attention of scientists for over 100 years. Backscattering occurs when the incident wave is reflected back in the same direction of incidence. In his work, Bragg [15] developed a backscatter relationship

for electromagnetic wave incident on a crystal. For a given periodicity Λ, an incident angle θ (at which the incident wave has an m-th order backscatter), and the wavelength of the incident wave λ, the backscatter geometry relation for a periodic surface is given as

$$m\lambda = 2\Lambda sin\theta \qquad [1]$$

with m the diffraction order (integer).

Ultrasonic studies conducted on periodic surfaces in 1970s showed that the relationship was also valid for ultrasonic waves. Experimental results by Quentin et al. [16] showed that when surfaces with periodic grooves (i.e. one-dimensional periodicity) were ensonified with narrow-band ultrasonic wave pulses, a maxima in the backscattered intensity are observed at very specific angles of incidence as shown in Figure 3; these angles can be predicted by Equation 1. This behavior can be explained by the diffracted modes that are generated at specific angles, because the periodic surface functions as an acoustic diffraction grating. These diffraction angles are predicted by the classical grating equation [17]:

$$m\lambda = \Lambda sin\theta_m - \Lambda sin\theta_i \qquad [2]$$

where θ_m is the diffracted angle and θ_i is the incident angle. It can be observed that Equation 1 simply constitutes the backscatter form of Equation 2. Figure 2 provides a schematic diagram showing the relationship of the various diffraction orders of the classical grating equation.
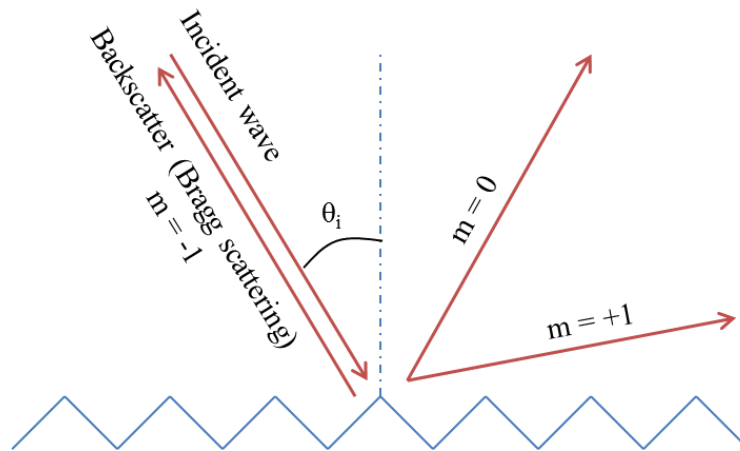
Figure 2: Schematic showing the physical representation of the different diffraction orders in the classical grating equation
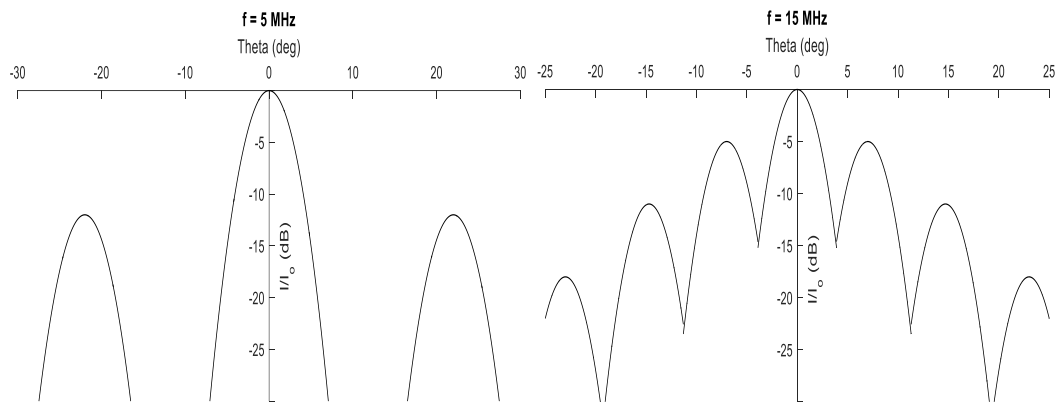
Figure 3: Reproduction of backscattering diagrams from "Narrow-band" experiments carried out by Quentin et. Al. [16] for a surface diffraction grating of $\Lambda = 0.0004$m for two different frequencies

Quentin et al. proved that as the frequency of the incident narrowband pulses increases, more backscattered modes can be observed for a given angular range. As a result, if the angular locations of these backscattered modes are examined for several frequencies, accurate predictions can be made about the surface periodicity [17]. Furthermore, the study was extended to broadband pulses to determine the spectral signatures of rough surfaces in both 1-D and 2-D periodicity [18]. The value of the Bragg angle was used to determine the periodicity, while the backscattering intensity was found to relate to the RMS value of the

surface roughness. This was validated by experimental results by Blessing et. al. [19] which showed that the amplitude of the diffraction peak at the Bragg angle incidence increased with increasing corrugation height for a given periodicity.

Ultrasonic characterization at the Bragg regime has become a key method in nondestructive testing and analysis of the surface structure of rough or corrugated surfaces [20]. However, certain anomalies may be observed with regards to the backscattered frequency spectra. Wood anomalies (similar to the optical spectra) were shown to exist in the normal incidence reflection spectra for an ultrasonic beam on a corrugated surface; sharp discontinuities or valleys appeared at certain frequencies in the spectrum [21]. This can be explained due to the mode conversion from bulk to surface waves on the periodic surface [17]. These "ghost" frequencies were shown to correspond to the diffraction orders along the surface with Rayleigh wave velocity [21]. In another study by Mampaert et. al. [22], this presence in anomalies at different frequency locations was used to predict the periodicity of the profile. It can be noted that the studies in [21,22] were only carried out for a normal incidence reflection spectra. However, ultrasonic studies of periodic surfaces must consider the possible generation of Rayleigh surface waves or Lamb waves (in case of thin plates) if the diffracted modes match in phase with these other modes [17].

This study with AcoustiCode tags mainly considers backscattering at the Bragg regime for a narrowband frequency spectrum. In order to avoid interference with the Rayleigh/Lamb waves, AcoustiCode tags are designed such that the Bragg regime does not fall in the same angle(s) as these surface wave's critical angle. Hence, these anomaly effects are not taken into account for developing the theory and simulation. The effect of surface wave mode conversion on experimental results is considered in Section 5.1.

2.4   Problem Formulation

Given the need for a passive, acoustic, information encoding marker system for navigation, a solution is proposed which combines the backscattering characteristics of periodic surfaces, and the benefits of a side-scan SONAR. The purpose of this work is to develop and test tags that are designed with varying periodic surfaces to encode positioning information through the variances in their backscattered regime. Based on the unique scattered pressure seen from the tag for an incident beam geometry, an acoustic signature can be created. This thesis develops the theory with regards to the 3-D scattered pressure that is observed upon a sidescan SONAR beam incident on a periodic 2-D tag surface. A coordinate system and an angle convention is defined, and the effect of SONAR beamwidth and bandwidth are also taken into account. A simulation model is utilized to analyze the variances in the backscattered pressure for different tag shapes to understand what constitutes an ideal tag that can be used for encoding acoustic information. Using the simulation results, a navigation/positioning method is proposed to obtain the location of the SONAR with respect to a given tag. Finally, AcoustiCode tags are designed and experimental data is collected in a water-tank to analyze the performance of these tags.

CHAPTER III

THEORY

3.1 Bragg Backscattering

For an ultrasonic sound wave incident on a periodic surface, the Bragg backscattering theory given by Equation 1 can be used to predict the angles at which constructive interference results in higher backscattered intensities at the receiver. When the path difference is equal to an integer number of wavelengths, constructive interference occurs. Figure 4 illustrates the geometry of the reflection that occurs for a plane wave incident on a periodic surface at Bragg angle.
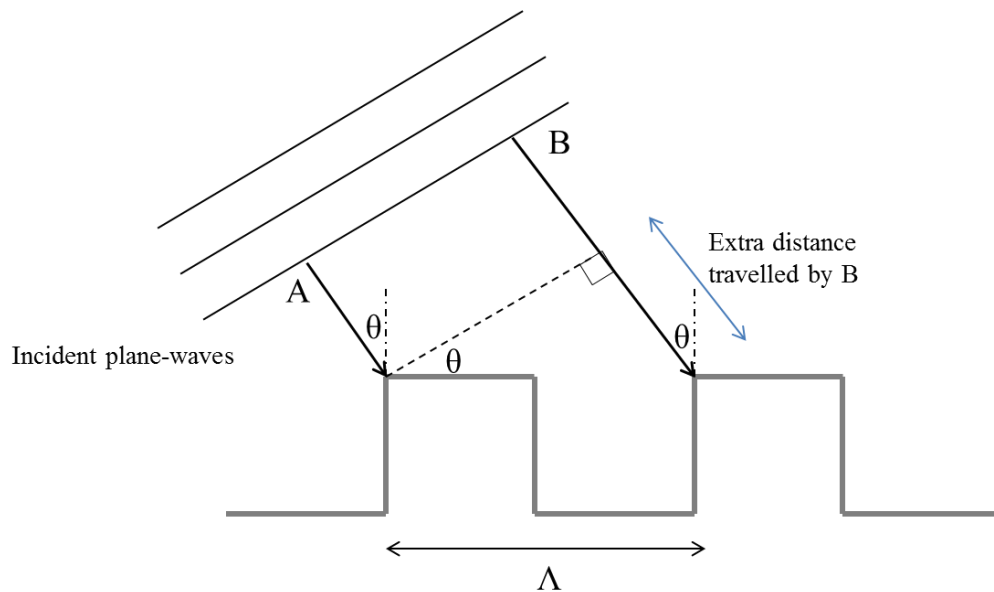
Figure 4: Plane-wave backscattering at Bragg angle from a periodic surface

The wave front approaches the periodic surface at an angle of incidence θ measured from the vertical of the surface to the perpendicular of the wave front. Point *A* on the wavefront impacts the surface first and the extra distance travelled by point *B* as compared to point *A* can be calculated as $2\Lambda sin\theta$. If this distance is an integer multiple of the wavelength, then point *B* of the wave-front will travel towards the surface, impact the surface and reflect back, to arrive in phase with point *A* of another wave-front. The reflected wave fronts will propagate back and impact the receiver at the same time leading to constructive interference. A given spacing Λ will produce constructive interference at an angle θ_{bragg} determined by Bragg's Law, as seen in Equation 1.

This section develops the theory with regards to the scattering that is observed for an acoustic plane-wave incident on a finite-size 2-D periodic surface such as that of an AcoustiCode tag. The effect of beamwidth of the SONAR and bandwidth considerations are also included in order to better simulate the real-world scenario.

3.2   *Co-ordinate systems and Conventions*

The co-ordinate systems used in subsequent sections are dependent on the two main components of the SONAR-tag navigation system: SONAR co-ordinate system (SCS), and tag co-ordinate system (TCS). Figure 5 represents a typical SONAR and AcoustiCode tag system that would be used. Since the side-scan SONAR acts as the emitter and the receiver, and the tag is always observed with respect to its position, SCS can be treated as the fixed frame.
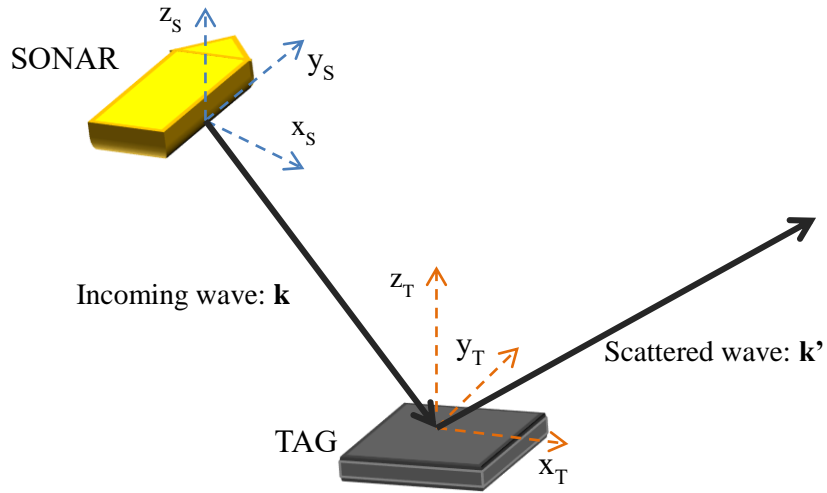
Figure 5: SONAR and Tag co-ordinate systems definition with the notation for the wavenumber k and k' of the incoming and scattered waves respectively

The SCS origin is located at the geometrical center of the fin of the side-scan SONAR, from where the SONAR beam originates and spreads out towards the tag. The TCS origin is located at the center of the 2-D tag (in the x-y plane). The beam incident on the tag is represented as a 3-D vector k, whereas the scattered beam out of the tag is represented as a 3-D vector k'. To analyze the scattered beam, the incident beam geometry has to be converted from SCS to TCS by using a combination of rotation and translation matrices, depending on the positional difference between the tag and the SONAR.

Figure 6 shows the angle convention that is used to characterize the directions of the incident and scattered wave vectors with respect to the tag co-ordinate system (TCS). The azimuth angle (with respect to x-axis) is given by Φ, and the elevation angle (with respect to z-axis) is given by θ.

13
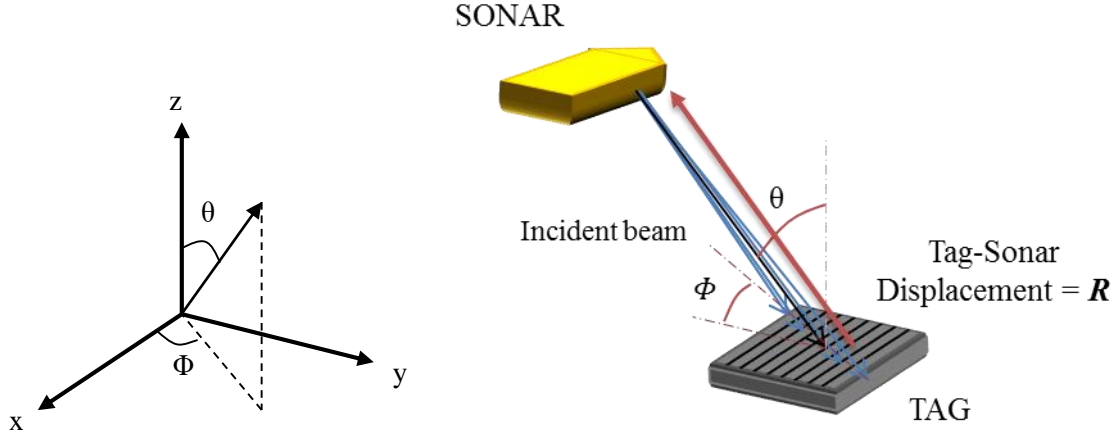
Figure 6: Angle convention for used for describing wave vectors in TCS

Hence, the rotation matrices used to convert the beam vectors from SCS to TCS can be given as a function of Φ and θ. Two main rotations have to be performed in z and y axis to account for the incoming beam's azimuth and elevation angles. The rotation matrices have to be multiplied by incoming beam vector in SCS, k_{SONAR}, to obtain the beam vector in TCS k_{TAG}, as shown in Equation 4 (k_{SONAR} and k_{TAG} are a representation of incoming beam k in SCS and TCS respectively).

$$R_y = \begin{matrix} \cos\left(\theta - \frac{\pi}{2}\right) & 0 & -\sin\left(\theta - \frac{\pi}{2}\right) \\ 0 & 1 & 0 \\ \sin\left(\theta - \frac{\pi}{2}\right) & 0 & \cos\left(\theta - \frac{\pi}{2}\right) \end{matrix} \qquad R_z = \begin{matrix} \cos(\Phi) & \sin(\Phi) & 0 \\ -\sin(\Phi) & \cos(\Phi) & 0 \\ 0 & 0 & 1 \end{matrix} \qquad [3]$$

$$k_{TAG} = R_y * R_z * k_{SONAR} \qquad [4]$$

Given that this work involves a 3-dimensional incoming wave with an elevation angle θ and an azimuth angle Φ, Equation 1 can be extended to include the new adjusted periodicity assuming that the tag is periodic along x axis (i.e. a slice of tag across x axis is periodic). Figure 7 and Equation 5 describe how the apparent periodicity can be obtained.
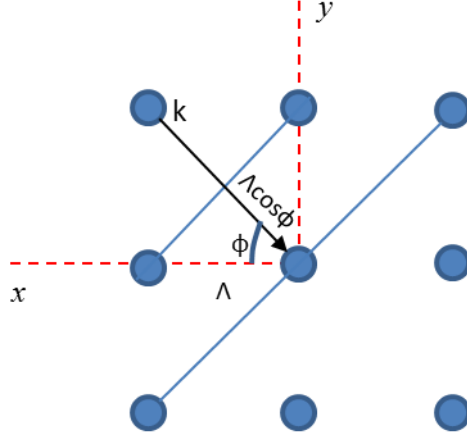
Figure 7: Schematic diagram showing plane waves with the wave vector k incident on the periodic tag at a given azimuth angle Φ

Given the geometry shown in Figure 7, the apparent periodicity adjusted to include the azimuth angle Φ is given as Λ_Φ shown in Equation 5. Hence, Equation 6 is obtained as an extension of Equation 1.

$$\Lambda_\Phi = \Lambda cos\Phi \tag{5}$$

$$m\lambda = 2\Lambda cos\Phi sin\theta \tag{6}$$

3.3 Scattering Equation for a Periodic Surface

3.3.1 Spatial Fourier Transform of 2-D Binary Tag

For any arbitrary 2-D periodic surface tag, its periodicity and shape can be expressed as a spatial density function with respect to the geometric axes, $\rho(x, y)$. An example is shown in Figure 8a, where the tag is represented as a binary density function i.e. the white surface or the '1's' represents the reflecting portion of the tag, whereas the black surface or the '0's' represents the non-reflecting portion. The intensity and direction of the scattered waves k' given an incident wave k on the tag can be analyzed by breaking down this density

15

function into its spatial frequency components. A Fourier transform of the density function in space is taken, as shown in Equation 7.

$$n_G(G_x, G_y) = \int_{-y}^{y} \int_{-x}^{x} \rho(x, y)\, e^{-2\pi i(k_x x + k_y y)}\, dx\, dy \qquad [7]$$

For the tag shown in Figure 8a, using Equation 7, a spatial Fourier transform of the tag can be computed to analyze the spatial frequencies observed in the tag. Figure 8b shows a magnified portion of the scaled image plot for a 2-D spatial FFT performed on the tag shown in Figure 8a; the FFT data has been normalized with respect to the maximum value. If we take a slice of this plot at $k_y = 0$, we obtain Figure 8c; in this figure, the different peaks are indicative of the strength of a particular spatial frequency seen in the tag, and the direction of periodicity they correspond to.
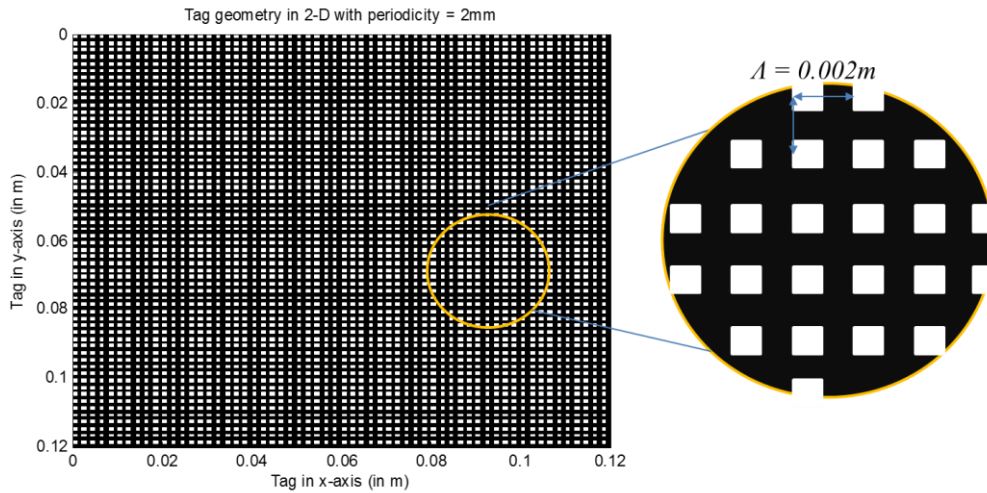
(a)

Figure 8: a) Arbitrary tag geometry in *x-y* axis, b) Spatial FFT of tag, c) Slice of the spatial FFT at $k_y = 0$

16

Spatial FFT of tag in 2-D

X: 0 Y: 500
Index: 0.6392
RGB: 1, 0.938, 0

X: 500 Y: 500
Index: 0.4086
RGB: 0.188, 1, 0.813

X: 500 Y: 0
Index: 0.6392
RGB: 1, 0.938, 0

Wavenumber in y-axis - k_y (1/m)

Wavenumber in x-axis - k_x (1/m)

Amplitude relative to max at (0,0)

(b)

Slice at $k_y = 0$

Spatial FFT of tag in 1-D

$G_{xi} = 500$
$G_{yi} = 0$
$n_{Gi} = 0.64$

$G_{xi} = 1000$
$G_{yi} = 0$
$n_{Gi} = 0.08$

Normalized Spatial FFT Amplitude

Wavenumber in x-axis - k_x (1/m)

(c)
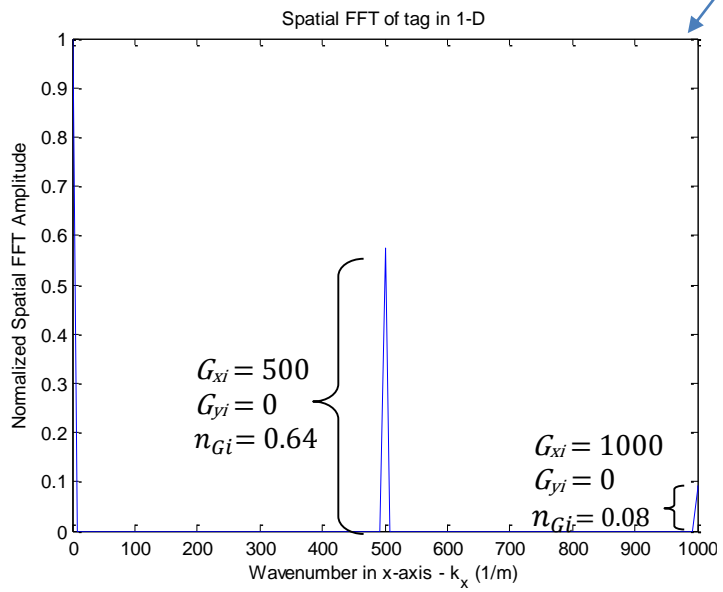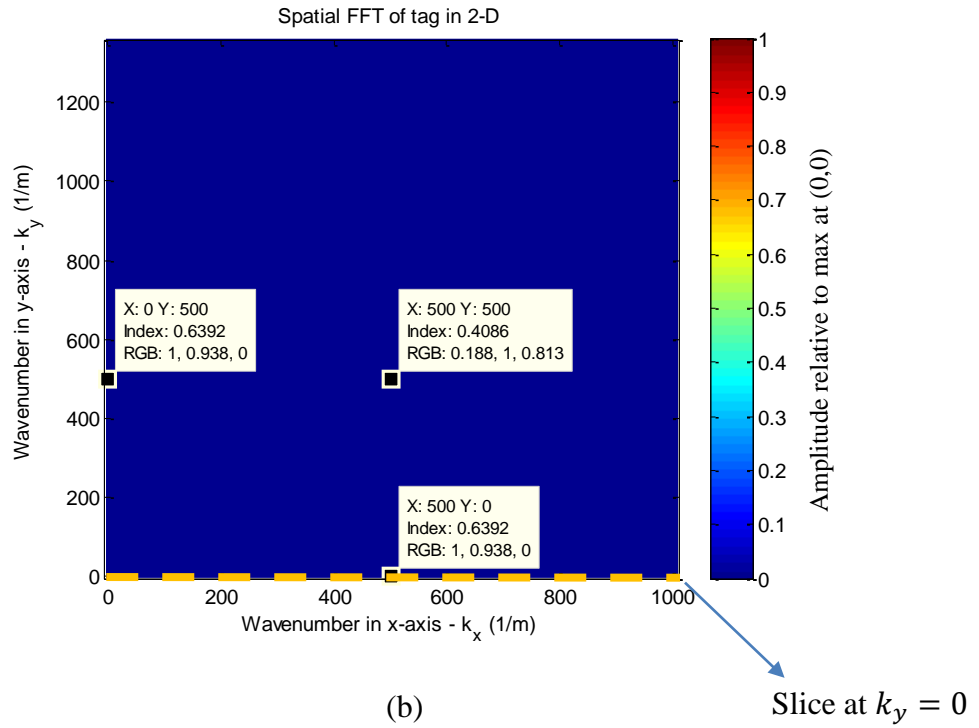
Figure 8 continued

17

For a 2mm periodicity grid tag shown in Figure 8a, the periodicities are primarily seen in x-axis (unit vector of $\begin{bmatrix} 500 \\ 0 \end{bmatrix}$ m^{-1}), y-axis (unit vector of $\begin{bmatrix} 0 \\ 500 \end{bmatrix}$ m^{-1}), and at the diagonal (unit vector of $\begin{bmatrix} 500 \\ 500 \end{bmatrix}$ m^{-1}). For different tag shapes, the magnitude and direction of these spatial frequencies may vary.

Each of the directions in which periodicities are observed can be represented as a set of vectors $\boldsymbol{G}$, and their corresponding amplitudes can be represented as n_G (as defined in Equation 7). In Figure 8b, each point can be written as an x-y vector representation given as $\boldsymbol{G_i}$, and corresponding amplitude given as n_{Gi}. An example has been shown in Figure 8c for $\boldsymbol{G_i} = \begin{bmatrix} 500 \\ 0 \end{bmatrix}$ m^{-1}, $\begin{bmatrix} 1000 \\ 0 \end{bmatrix}$ m^{-1}, and a corresponding n_{Gi} = 0.64, 0.08 respectively. Since most points in Figure 8b have a n_{Gi} that is negligibly small, for ease of computation, the subsequent simulation model ignores those points and only considers the peaks above a threshold $n_{Gi} > 0.01$ (i.e. 1% of the maximum n_{Gi}).

3.3.2 Scattered Wave Amplitude

Given the notation for incident wave ($\boldsymbol{k}$), possible scattered wave directions ($\boldsymbol{k'}$), and the tag periodicity descriptors ($\boldsymbol{G}$, n_G), the next step is to analyze how the scattered beam propagates through the scattered directions. Figure 9 shows the schematic diagram for the incident beam and the scattered beam falling on an area element dA of the tag which is a displacement $\boldsymbol{r}$ from the origin O of the tag. The total difference in phase angle between the incident and scattered beams can be denoted as $(\boldsymbol{k}\text{-}\boldsymbol{k'})\cdot \boldsymbol{r}$, and the wave scattered from dA at $\boldsymbol{r}$ has the the phase factor $\exp[i(\boldsymbol{k}\text{-}\boldsymbol{k'})\cdot \boldsymbol{r}]$. The amplitude of the wave scattered from an area element is proportional to the local periodic density $\rho(x,y)$. [23] Thus, the total

amplitude of the scattered wave in the direction k' is proportional to the integral over the tag of $\rho(x, y)\, dA$ times the phase factor $exp[i(k\text{-}k')\cdot r]$. This relationship can be represented by:

$$F = \int dA\, \rho(x, y)\, exp[-i(\Delta k).r] \qquad [8]$$

where $\Delta k = k - k'$, r represents the set of vectors defining any given point on the tag, and A represents the area of the tag.
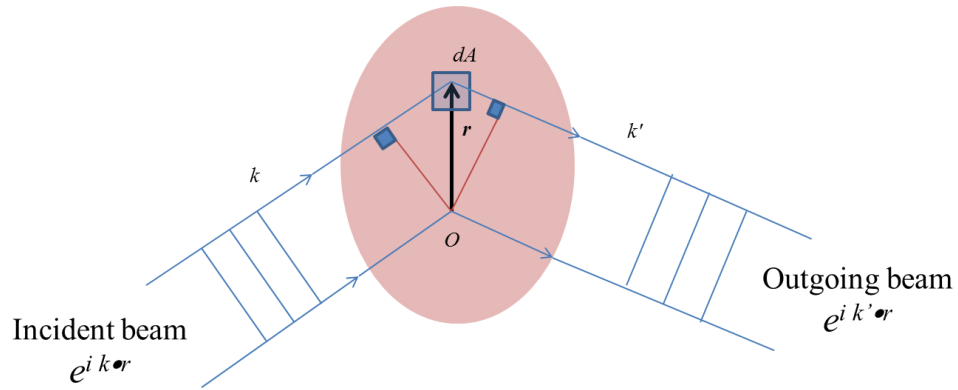
Figure 9: Schematic showing that the total difference in phase angle is $(k\text{-}k')\cdot r$ for area elements r apart

To calculate the scattered wave amplitude F, $\rho(x, y)$ in Equation 8 can be replaced by its Fourier components to obtain Equation 9; this formulation is adapted from the scattering amplitude derived by Kittel, C [23] for an incident x-ray beam diffracted by a crystal lattice.

$$F = \sum_G \int dA\, n_G\, exp[i(G - \Delta k).r] \qquad [9]$$

A simplified version of Equation 9 can be obtained in the Cartesian coordinates given that r exists in the x-y space as seen in the tag coordinate system:

$$F = \sum_G \iint dxdy\, n_G\, exp[i(G_x + k_x - k_x')x]exp[i(G_y + k_y - k_y')y] \qquad [10]$$

19

Since the origin of the tag coordinate system lies at the center of the tag, the integrals in Equation 10 can be bounded from $-L/2$ to $L/2$ for a rectangular tag:

$$F = \sum_G n_G \int_{-\frac{L_x}{2}}^{\frac{L_x}{2}} exp[i(G_x + k_x - k_x')x]dx . \int_{-\frac{L_y}{2}}^{\frac{L_y}{2}} exp[i(G_y + k_y - k_y')y] dy \quad [11]$$

Upon solving the integrals in Equation 11, the scattering Equation for a periodic surface is obtained, as shown in Equation 12; it describes the scattered amplitude for a wave scattered in the direction k' given a periodic surface tag in the x-y plane with an incoming wave k.

$$F = \sum_G n_G L_x L_y \, sinc\left[(G_x + k_x - k_x')\frac{L_x}{2}\right] sinc\left[(G_y + k_y - k_y')\frac{L_y}{2}\right] \quad [12]$$

For the case shown in Figure 6, the scattered amplitude F calculated by Equation 12 has to be propagated up to the receiver that is located at a displacement R from the tag in order to calculate the pressure observed back at the SONAR.

$$P = Fe^{i(k' \cdot R)} \quad [13]$$

3.4 Beamwidth and Bandwidth considerations

A typical side-scan SONAR emits a beam with a width of 1-2° in the horizontal [20], as shown in Figure 1c. In case of the Tritech StarFish 452F used in this study, the side-scan SONAR emits a beam with a beamwidth of 0.8° (-3dB signal level), and the chirp frequency range is from 430-470kHz [23]. Due to the given beamwidth Δ_{beam}, a beam falling entirely on the tag will contain multiple incident plane waves falling on the tag at different angles, as shown in Figure 10.
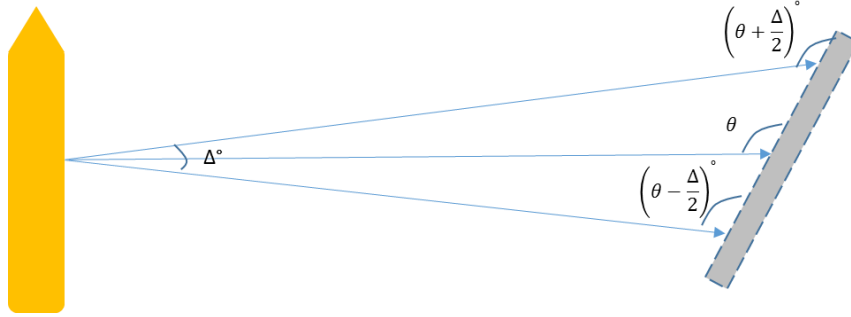
Figure 10: Schematic showing the effect of beamwidth on incidence angle at the tag
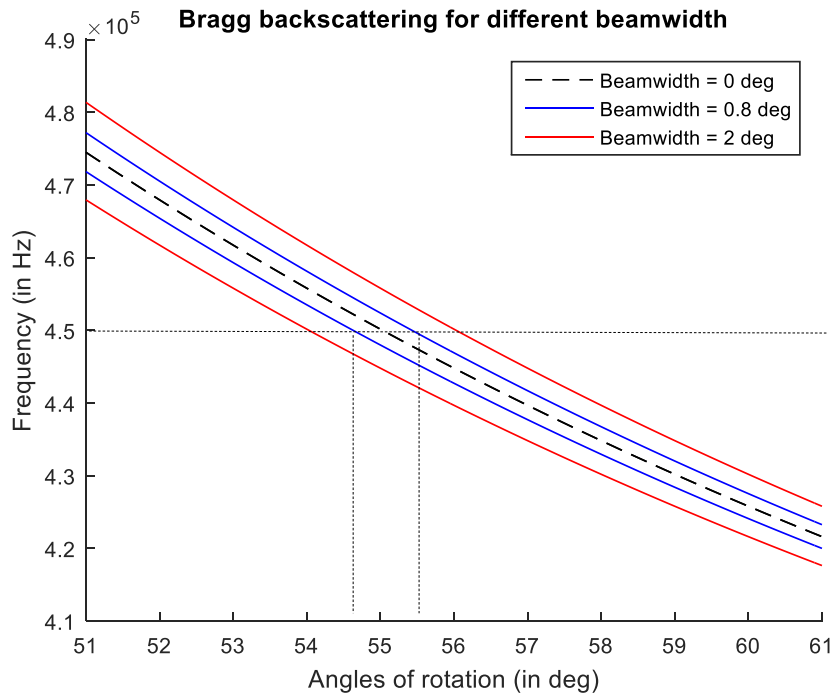
Figure 11: Plot comparing Bragg angle range observed for different incident beamwidths for a 2mm periodicity tag

The variation in the incident angles seen at the tag leads to a range of elevation angles, θ.

Figure 11 plots Equation 1 while accounting for this variation in θ for different beamwidths

(assuming that the beam falls within the tag). The SONAR frequencies replace the

corresponding λ in Equation 1, and a θ vs frequency plot is obtained for $\Lambda = 2mm$ and speed

of sound in water $c = 1500m/s$. For a beamwidth of 0.8°, at 450 kHz, the Bragg

backscattering may be observed from $\theta = 54.5°$ to $55.5°$. When extended to the entire the entire bandwidth of 430-470kHz, this Bragg backscattering range increases from $\theta = 51.2°$ to $59.5°$. Hence, bandwidth and SONAR beamwidth effects of the incident beam need to be incorporated into the simulation due to their influence on the extent of the Bragg regime.

The beam emitted from the side-scan SONAR can be modelled as a collection of a number of N discrete multiple plane waves, each travelling in different directions within the beamwidth angle Δ_{beam}, as shown in Figure 12a. Since the strength of these plane waves decreases with increasing beam angle Δ, the beam can be described as a typical Gaussian function given in Figure 12b. The resultant beam is shown in Figure 12c.

(a)   (b)

(c)
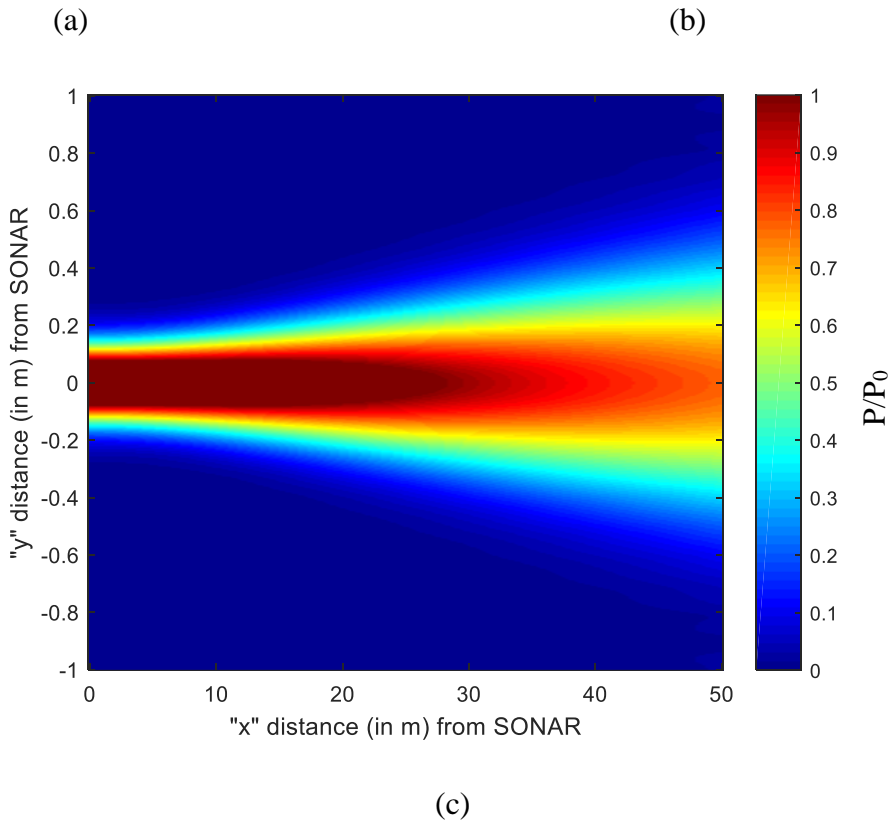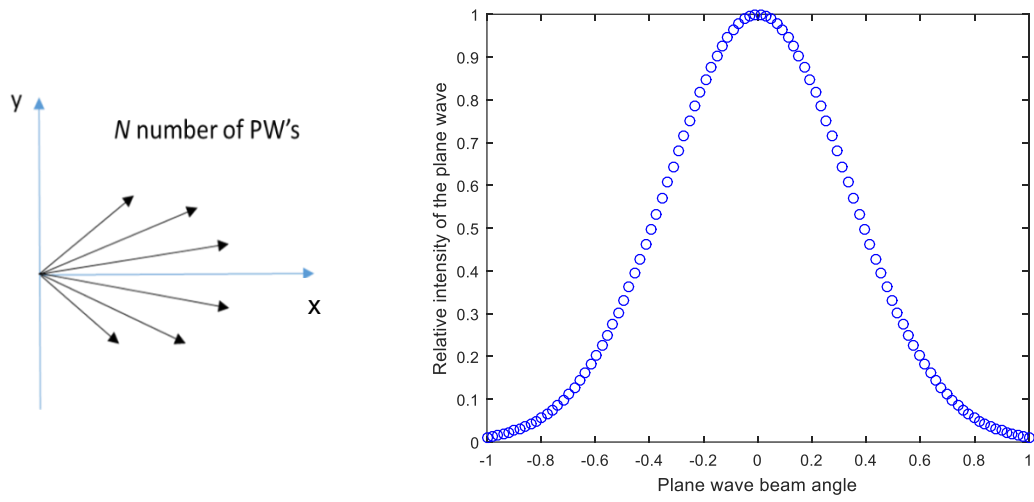
Figure 12: a) Schematic of plane waves emitted from the SONAR, b) Relative strength of plane waves with varying Δ_i (normalized by the maximum) for $\Delta_{beam} = 2°$, c) SONAR beam pressure amplitude as seen in the x-y plane for $\Delta_{beam} = 2°$

Each plane wave in Figure 12a can be described in terms of its direction and its relative intensity. Given a particular radial frequency ω and the speed of sound in water c, the direction components of each plane wave can be calculated using Equation 14.

$$k_{xi} = \frac{\omega}{c} cos\Delta_i \,,\, k_{yi} = \frac{\omega}{c} sin\Delta_i \qquad [14]$$

When simulating the beam, it is vital to consider aliasing issues that may arise as discussed in Appendix A. This interference occurs due to sampling issues in the k_y or Δ space. A small enough sampling period $\delta\Delta$ has to be taken for simulating the tag upto a maximum distance R_{max}.

By combining the scattering equation for a periodic surface (Equations 12, 13) along with the SONAR beamwidth and the bandwidth effects, the next chapter develops a numerical simulation in order to predict the Bragg scattering that would be obtained in a 3-D domain. The theoretical 3-D Bragg scatter equation derived in Equation 6 is used to validate the model.

CHAPTER IV

NUMERICAL SIMULATIONS

4.1   Simulation Framework

A simulation framework was developed in order to predict the scattered wave pressure (calculated using Equation 13 in Section 3.3) that would be observed back at the SONAR for a given incident beam as described in Figure 13. Appendix B describes the overall simulation process flow. To accurately represent the StarFish 452F SONAR beam (see Figure 1a), simulated data were generated for a beamwidth Δ_{beam} of 0.8° (similar to Figure 12) and a frequency bandwidth ranging from 430-470 kHz.

The simulated beam is first discretized into N multiple plane waves within the beamwidth (as shown in Figure 12, 13) such that the sum of the energies of all the plane waves is always equal to 1. Similarly, the sum of energies of all the discretized frequencies in the bandwidth is normalized to always equal to 1. This allows for an accurate comparison of the scattered pressure result relative to the incident beam energy.

The scattered amplitude in Equation 12 was calculated for each of the discretized frequencies and plane waves. At each frequency, the pressure amplitude was calculated by summing up the scattered amplitudes for all the set of discrete plane waves. Hence, Equation 13 becomes:

$$P = \sum_{j=1}^{N} F_j e^{i(\boldsymbol{k'} \cdot \boldsymbol{R})} \qquad [15]$$
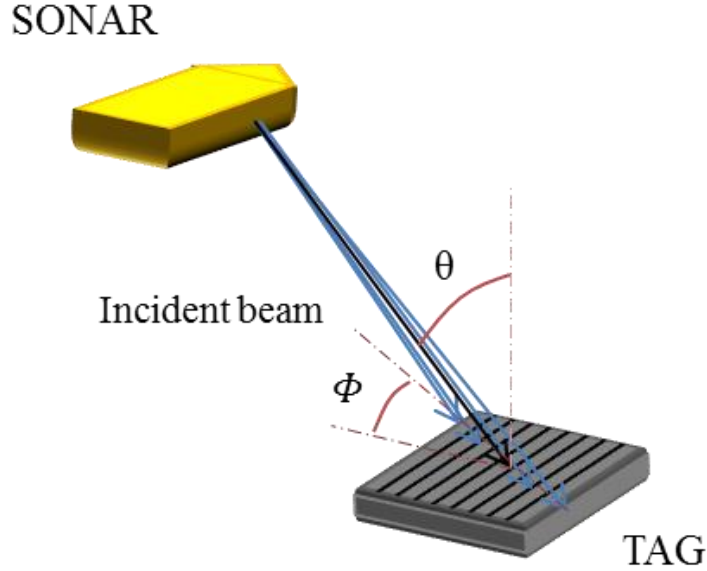
SONAR

Figure 13: Geometry of the periodic tag ensonified by a SONAR beam centered on an
elevation angle θ, and azimuth angle Φ

4.2   Comparison of Different Tag Geometry

Different types of tags with varying periodicities and shapes were simulated to compare
and understand which tag is ideal for encoding acoustic information. Three types of
periodic 2-D tags investigated using this simulation were – ridge tag (Figure 14a), grid tag
(Figure 15a), circular tag (Figure 16a). The tags constructed in the simulation are binary
periodic functions where in white represents 1's or reflecting surface (i.e. the top of a flat
groove or flat ridge), and black represents 0's or non-reflecting surface (i.e. the space in
between groove or ridges). The tags shown in Figure 14, 15, 16 have the same periodicity
Λ of 3mm. Upon substituting this Λ value in Bragg equation (Equation 1) for a speed of
sound in water $c = 1500 \ m/s$, and the center frequency $f_m = 450 \ kHz$, the Bragg elevation
angle θ_{bragg} is found to be 33.7°. Figures 14b, 15b, 16b show the resultant scattered pressure
(in dB drop) obtained back at the SONAR receiver (in the SONAR bandwidth) for the
respective tags. These results are obtained for varying elevation angle θ, whereas the

azimuth angle Φ is kept constant at 0°. A theoretical curve plotting Equation 6 is overlaid on the simulation results for validating the Bragg backscatter observation.

(a) (b)
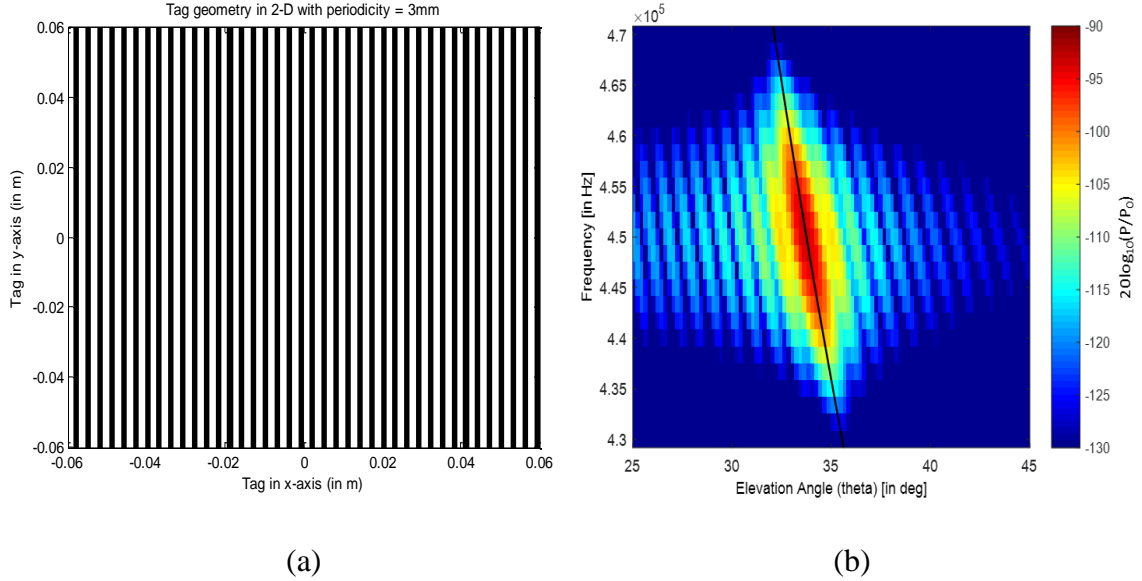
Figure 14: a) Ridge tag with periodicity $\Lambda = 3$mm; b) Scattered pressure amplitude (in dB drop) observed at the SONAR for varying elevation angles θ, azimuth angle $\Phi = 0°$ at the SONAR beam band for the given ridge tag

(a) (b)
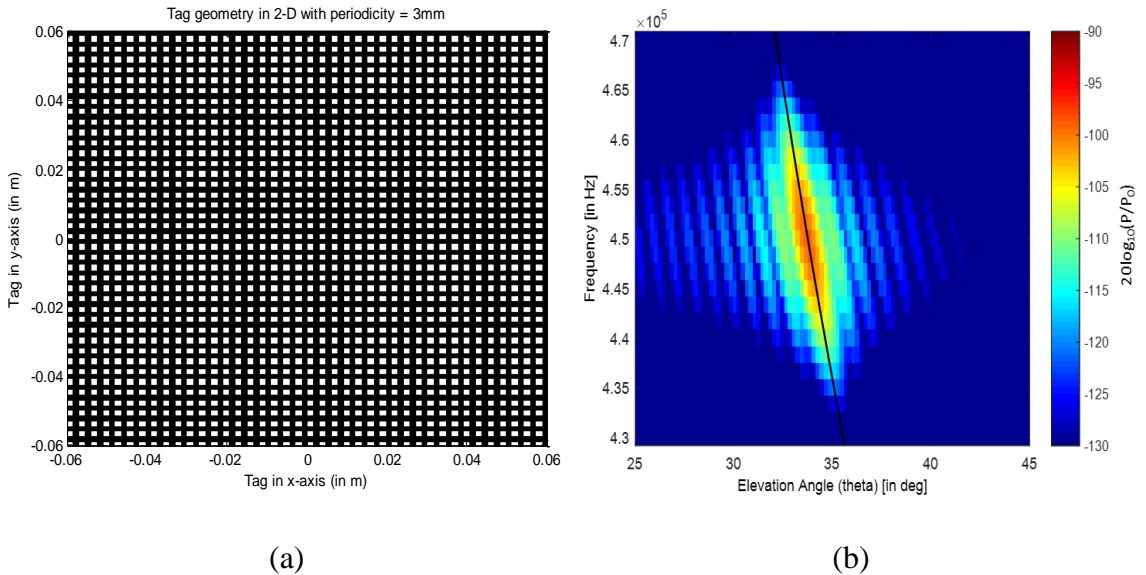
Figure 15: a) Grid tag with periodicity $\Lambda = 3$mm; b) Scattered pressure amplitude (in dB drop) observed at the SONAR for varying elevation angles θ, azimuth angle $\Phi = 0°$ at the SONAR beam band for the given grid tag
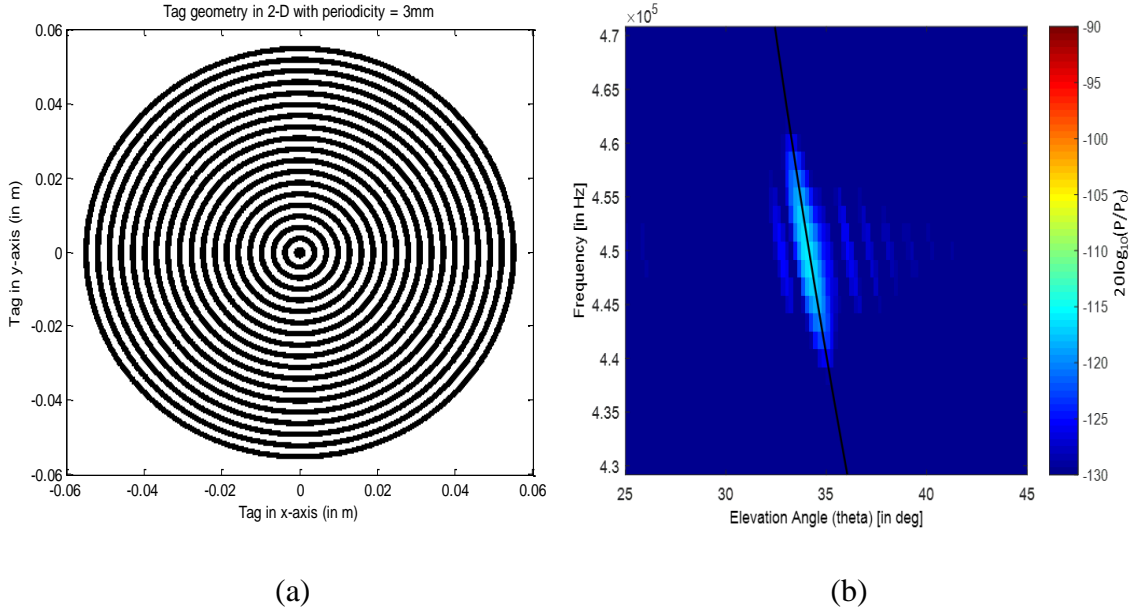
Figure 16: a) Circular tag with periodicity $\Lambda = 3mm$; b) Scattered pressure amplitude (in dB drop) observed at the SONAR for varying elevation angles θ, azimuth angle $\Phi = 0°$ at the SONAR beam band for the given circular tag

A Gaussian amplitude distribution is assumed for the variation of the SONAR amplitude spectrum across frequency band from 430kHz to 470 kHz; hence the results obtained in Figure 14b, 15b, 16b show a higher reflection at the center of the frequency band as compared to the edges of the frequency band. For all three tags, Bragg scattering is observed at the θ_{bragg} (Equation 1), for $\Lambda = 3mm$, speed of sound in water $c = 1500 \ m/s$, frequency ranging from 430-470kHz.

Figure 14b, 15b, 16b have been plotted on the same logarithmic scale to highlight the differences in reflected pressure amplitudes seen at the Bragg regime between the three types of tags. The ridge tag shows the highest reflection at the Bragg regime with a 20dB higher reflection than the circular tag. In this case, the incoming beam has a $\Phi = 0°$; thus the plane waves are invariant along y axis, i.e. the wave vectors only have x and z components, and no y components. The ridge tag has a high density $\rho(x, y)$ of periodicity

28

in the x direction as compared to the other tags, hence leading to a higher value of n_G (see Equation 7) in the G_x direction. This results in a higher backscattered amplitude (calculated using Equation 12) for the ridge tag.

4.3 Influence of Azimuthal Directionality

Unlike the ridge tag, the circular tag has the same periodicity in all directions in the x-y plane. Therefore, even when $\Phi \neq 0°$, the scattered amplitude from a circular tag stays the same; however, the scattered amplitude for the ridge tag decreases as Φ moves away from $0°$ since the x component of the beam vector decreases. Figure 17 compares the scattered amplitude obtained for a ridge tag versus a circular tag (plotted on the same scale) at an azimuth angle $\Phi = 30°$ and varying elevation angles θ.

(a)
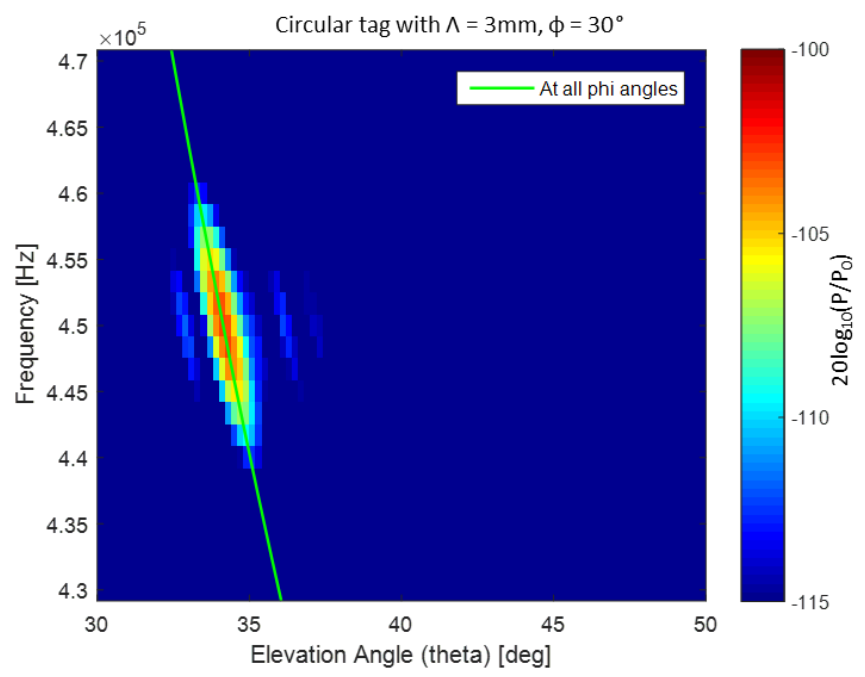
(b)

Figure 17: Scattered pressure amplitude observed at the SONAR for varying elevation angles θ, azimuth angle $\Phi = 30°$ at the SONAR beam band for a) ridge tag with periodicity $\Lambda = 3$mm; b) circular tag with periodicity $\Lambda = 3$mm. (Both (a) and (b) are plotted on the same scale)
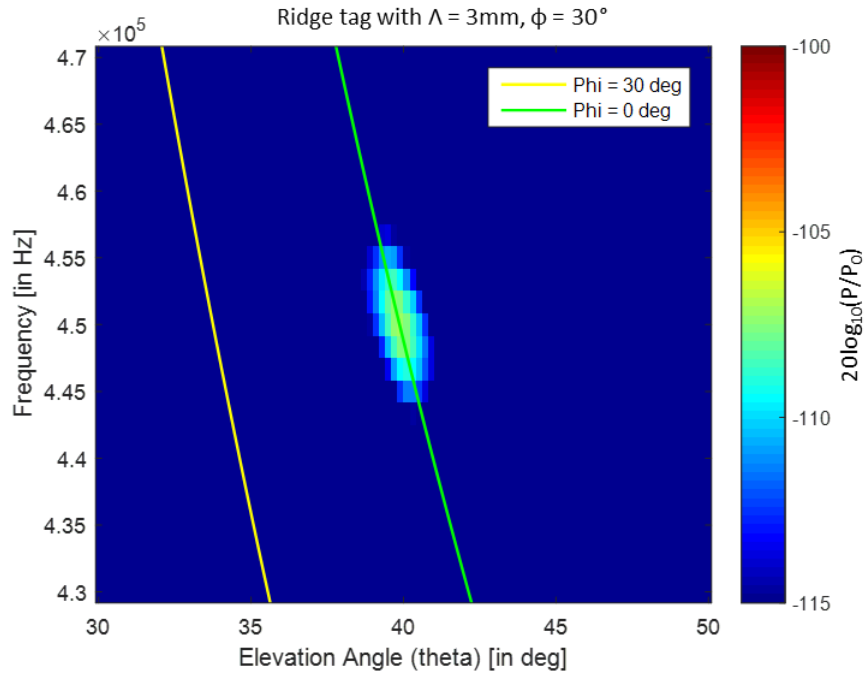
In contrast to Figure 14b, 16b (obtained for $\Phi = 0°$), Figure 17 suggests that the scattered pressure amplitude at the Bragg angle is greater for the circular tag versus ridge tag at $\Phi = 30°$. This happens since the periodic density $\rho(x, y)$ of ridge tag at $\Phi = 30°$ ends up being lesser than that of the circular tag. Figure 18a also suggests that as the azimuth angle Φ varies, the periodicity of the tag also changes leading to a shift in the Bragg regime. This behavior is explained by Figure 7 and Equations 5-6 (Section 3.2). For $\Phi = 30°$, $\Lambda_\phi = \Lambda cos\phi = 3cos30° = 2.6$ mm; hence, new Bragg elevation angle θ_{bragg} at the median frequency f_m is calculated to be 39.8°.

4.4 Using AcoustiCode for Navigation Applications

In order to utilize AcoustiCode tags to navigate, they have to be able to relay information about the bearing of the SONAR with respect to the tag. Given the behavior of ridge tags as shown in Figure 17, where in the apparent Bragg angle shifts with varying Φ, a navigation method can be developed to obtain the accurate position of the SONAR orientation with respect to the tag by identifying θ and Φ from the frequency dependence of Bragg angle.

A simulation was carried out for the ridge tag shown in Figure 14a to understand the variations in the apparent Bragg angle as the azimuth angle Φ of the incident SONAR beam varies. Figure 18 shows the simulated variations of the peak scattered pressure (in logarithmic scale) behavior of the ridge tag in the 3-dimensional domain as a function of θ and Φ.
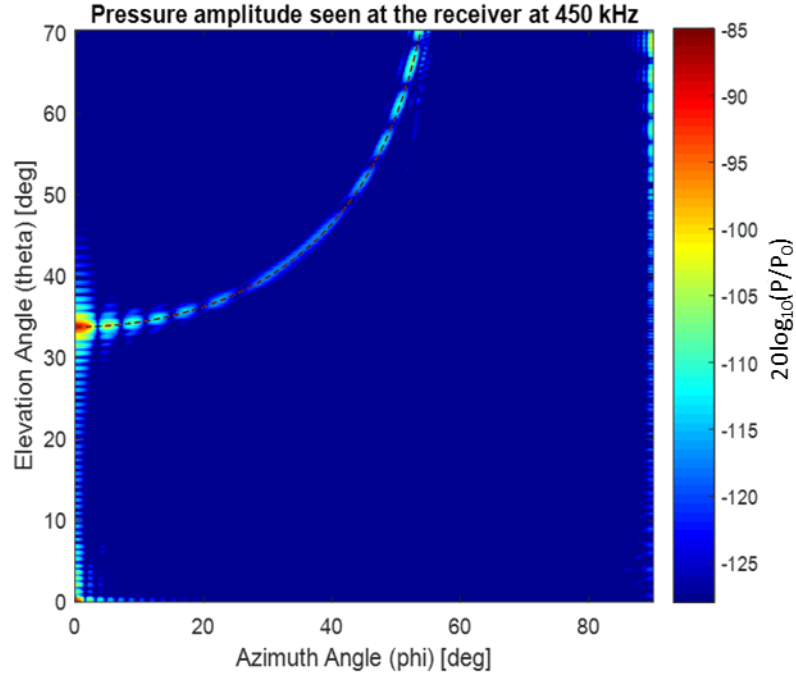
Figure 18: Scattered pressure amplitude in dB drop observed at the SONAR for ridge tag
with periodicity Λ = 3mm at 450 kHz

In Figure 18, Bragg scattering is observed at the apparent θ_{bragg}, described in Equation 6.
The relationship between elevation angle and azimuth angle for the Bragg scattering can
be given as:

$$sin\theta = \frac{m\lambda}{2\Lambda cos\phi} \qquad [16]$$

The dotted line shown in Figure 18 plots the relationship given in Equation 16. Figure 18
can be extended to include the Bragg response at other frequencies in the band. Figure 19a
plots the scattered pressure (in dB drop) behavior of the ridge tag in the 3-dimensional
domain as a function of θ and Φ for 3 different frequencies: 470 kHz, 450 kHz, 430 kHz
(assuming same energy input at each frequency). Given a broadband frequency, it becomes
easier to obtain the positioning information about the movement trajectory of the SONAR
if the type and the geometry of tag is known a priori. An example has been shown in Figure

32

19, wherein a given SONAR trajectory ends up creating a unique Bragg scattering return as seen by the SONAR.

(a)

(b)
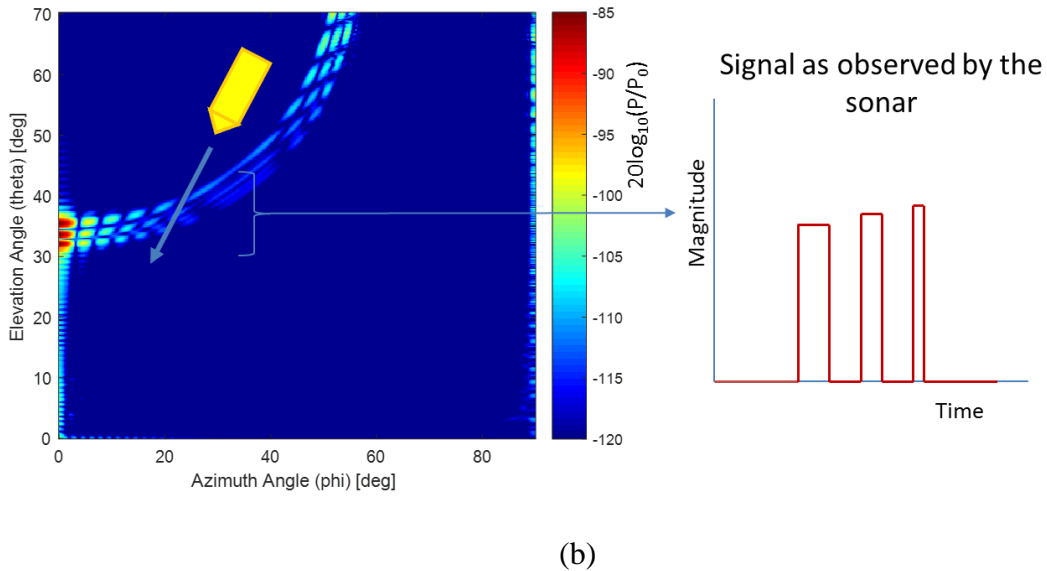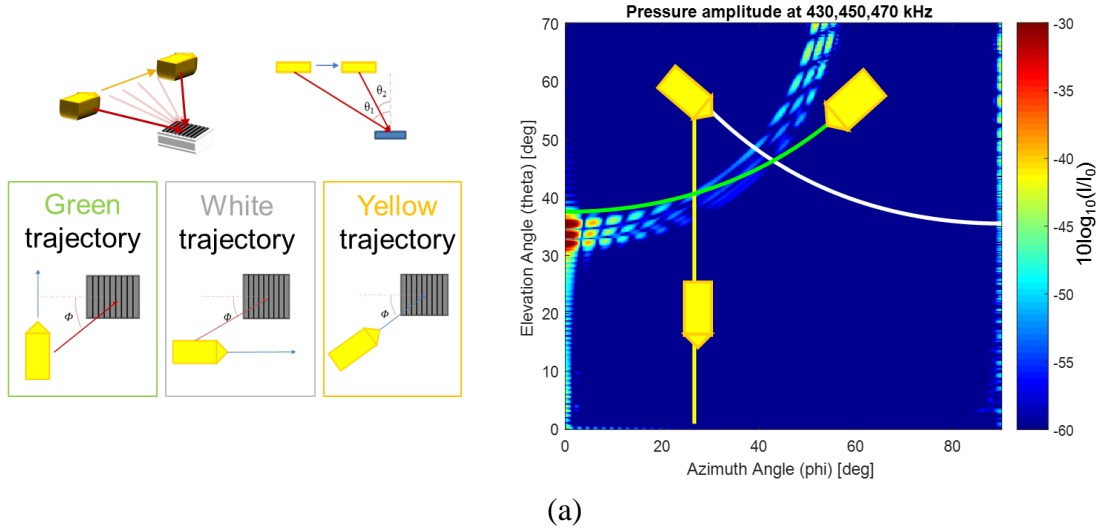
Figure 19: a) Three different SONAR trajectories overlay a 3-D scattered pressure amplitude map (in dB drop) observed at the SONAR for ridge tag with periodicity $\Lambda =$ 3mm at 430, 450, 470 kHz (furthest to closest from 0); b) Example of SONAR shown moving in an arbitrary direction with changing θ, Φ

In a case where the AcoustiCode tag is placed on the seafloor, the elevation angle to the tag can be estimated if the height of the SONAR with respect to the seafloor is known, and the range to the tag is measured. As the SONAR moves over the Bragg regime (as shown in Figure 19), the corresponding azimuth angle to the tag can be estimated for a known Bragg scatter response of the tag. Furthermore, the trajectories of the SONAR in Figure 19a creates a unique signal that is observed by the SONAR over the time domain; an example is shown in Figure 19b. Given a known Bragg scatter response of the tag for the SONAR frequency bandwidth, the signal obtained by the SONAR can be compared to the Bragg response (such as in Figure 19b) to obtain the SONAR's trajectory with respect to the tag.

4.5   AcoustiCode Tag for Encoding Information

To make the AcoustiCode navigation method more reliable and encode further information using the tag, an additional parameter can be added by using a ridge tag with multiple periodicities. Figure 20 shows the scattered pressure amplitude observed at the SONAR for varying elevation angles θ, azimuth angle $\Phi = 0°$ at the SONAR beam band for a ridge tag with 4 different periodicities $\Lambda = 2.0$ mm, 2.2 mm, 2.5 mm, 3.0 mm. Note that a normal specular reflection was also observed at $\theta = 0°$ (i.e. the SONAR beam is incident directly perpendicular to/on top of the surface of the tag).
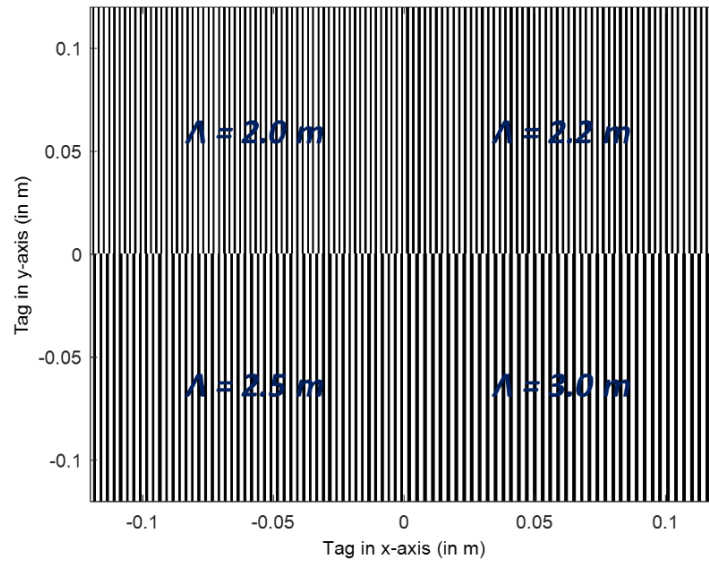
(a)
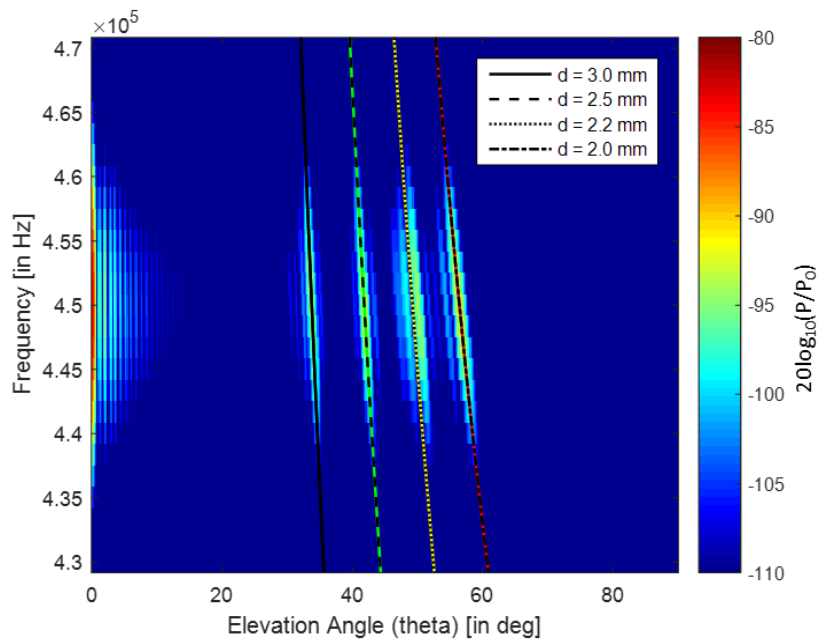
(b)

Figure 20: a) Ridge tag with 4 different periodicities Λ = 2.0mm, 2.2mm, 2.5mm, 3.0mm; b) Scattered pressure amplitude (in dB drop) observed at the SONAR for varying elevation angles θ, azimuth angle Φ = 0° at the SONAR beam band for given ridge tag

For the sake of simplicity, it was assumed that the four ridge tags were co-located within the beamwidth of the SONAR. By utilizing four different periodicities, 4-bit of information can be encoded into the tag, as compared to the 1-bit of information in a single periodicity tag (as seen in Figures 14-16). However, to utilize such a system, the SONAR will have to pass through all the elevation angles in the Bragg regime(s) of the tag.

The multiple periodicity tag can be used to reinforce the AcoustiCode navigation method described in Fig 18, 19a. Figure 21 adds extra bits of information to those shown in Figure 19a. This can be used to obtain a more accurate and precise tracking of the SONAR with respect to the tag, as it allows tracking of the SONAR over a wider range of θ, Φ.
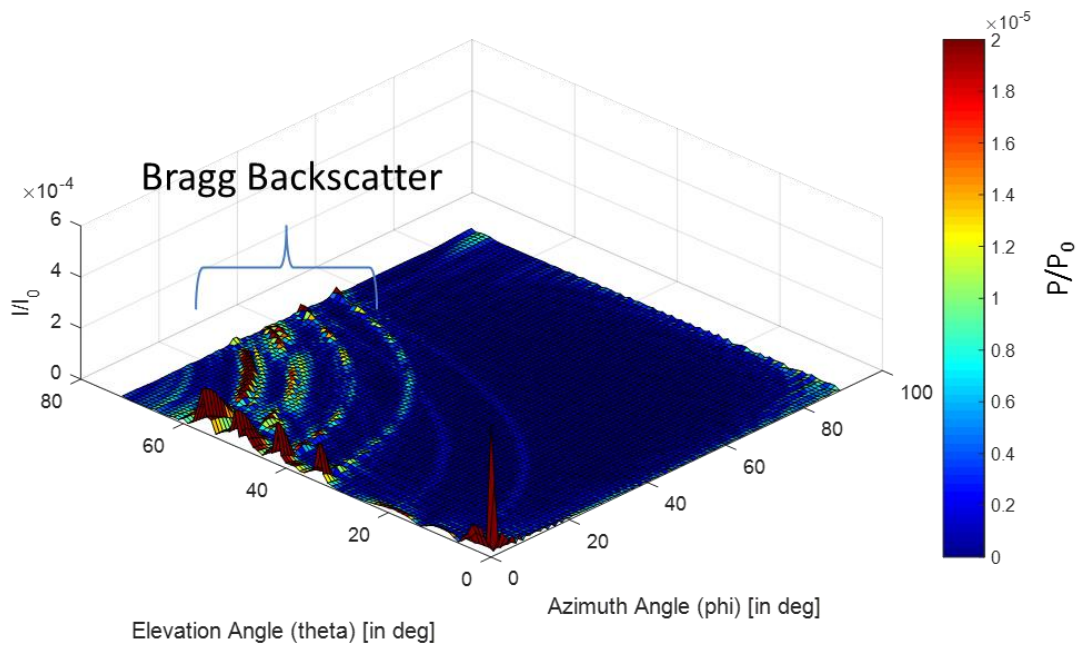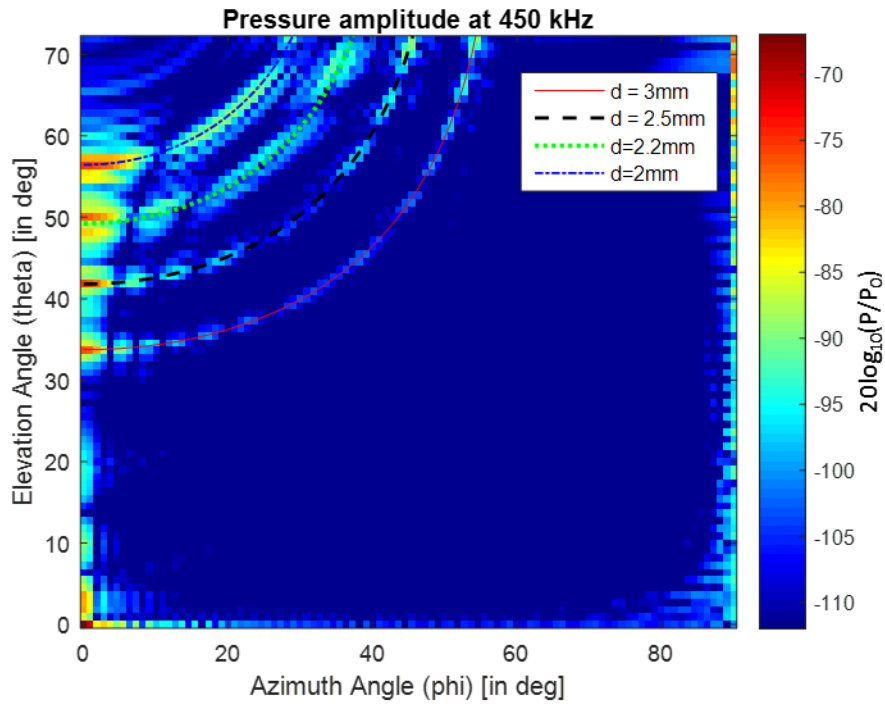
Figure 21: Scattered pressure amplitude observed at the SONAR for varying elevation angles θ, azimuth angles Φ for ridge tag with multiple periodicities $\Lambda = 2, 2.2, 2.5, 3$mm at 450 kHz

4.5   Conclusions

The results from the simulations validate the theory in Equation 6 suggesting that the Bragg regime is a function of both the elevation angle, and azimuth angle of the incoming beam incident on the tag. At $\Phi = 0°$, a tag with high periodicity density in the x direction (such as the ridge tag) shows the highest amplitudes of backscattered pressure. The circular tag always gives the same result for varying Φ, and becomes more efficient than the ridge tag as Φ moves further from $0°$. However, the ridge tag is chosen as the preferred tag, since it exhibits a large variation in Bragg regime over both θ and Φ. Given a broadband frequency, this result can be used to obtain positioning information about the movement trajectory of the SONAR by comparing the pressure return signal at the SONAR against the known Bragg regime similar to that in Figure19. Furthermore, multiple periodicities can be used to add extra bits of information to the tag.

Building on this simulation data, water-tank experiments are presented in the next section to:

1) Validate the Bragg scattering behavior experimentally
2) Compare the differences in backscattering amplitudes between a ridge tag and a circular tag
3) Understand the impact of different incident wave geometry by varying both elevation and azimuth angles of the incident beam
4) Test the use of multiple periodicities in a tag as a means to encode information

CHAPTER V

EXPERIMENTAL RESULTS

5.1 Experiment Setup and Tag Design

Experimental data were collected using Tritech Starfish 452F SONAR (operating specifications given in [27]) in a water tank measuring 10×8×8m (length × width × depth). Figure 22a shows a schematic diagram of the experiment setup in the tank. All the tags used for the experiments are made up of 3003 aluminum alloy and measure 120×120×3mm (length × width ×thickness). The sidescan SONAR and the tag were both submerged at the same depth of 1m below the water surface at a distance R apart. Care was taken to conduct the experiments such that the SONAR reflection from the water surface and from walls of the tank does not interfere with the tag data collection along the direct path; hence R was limited between $1.5m \leq R \leq 5.5m$ in order to avoid these interference.

In order to replicate the variation in the elevation angle, measurements were conducted as the tag was rotated about the z axis; a schematic diagram is shown in Figure 22b. At each sampled elevation angle, a SONAR chirp (from 430-470 kHz) was sent out by the Starfish 452F and the raw return signal (in voltage vs time) was measured by using a modified Starfish 450 Top Box (modifications shown in Appendix C) connected to a NI USB 5133 digitizer. The SONAR reflection signal was sampled at 50 Megasample/s for the time window chosen based on the distance to the tag. Equation 17 describes this distance as measured in time, t_{tag} i.e. the roundtrip time taken for the beam to travel to the tag and back.

$$t_{tag} = \frac{c_{water}}{2R} \qquad\qquad [17]$$
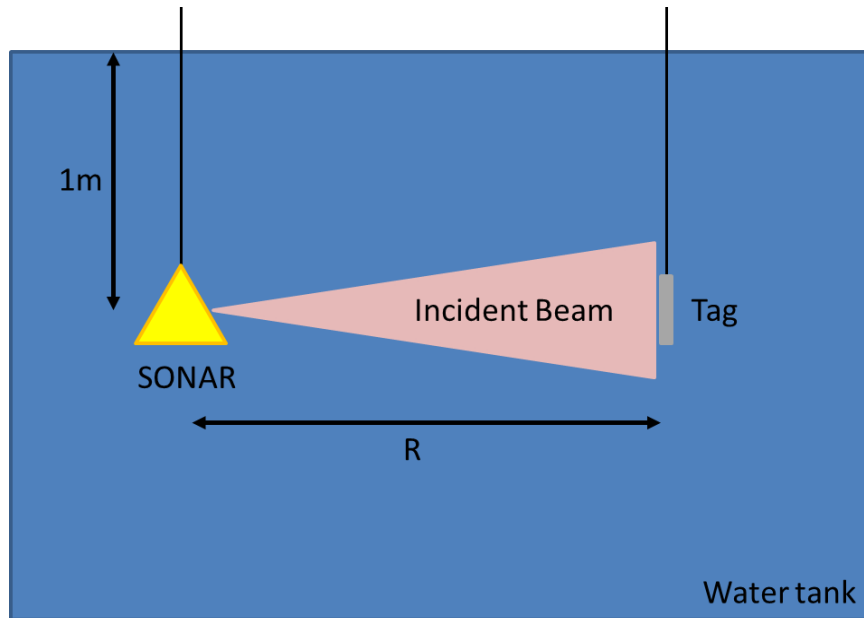
(a)
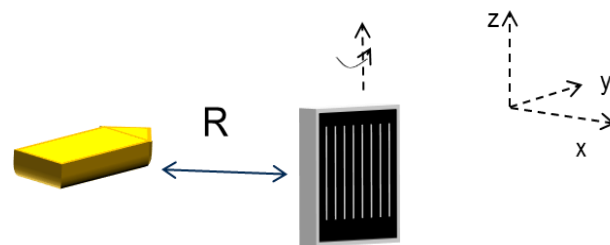
(b)

Figure 22: a) Schematic diagram of experiment setup in the water tank; b) Rotation of the AcoustiCode tag around z axis to replicate change in elevation angles θ

The time domain data collected from the NI USB 5133 digitizer was converted into the frequency domain by carrying out a Fourier transform of the time-voltage data. This is then plotted in the logarithmic scale for an easy comparison with the simulation results. Figure 23b illustrates the experimental result obtained for a control tag, which was simply a flat surface without any grooves or ridges (shown in Fig 23a).
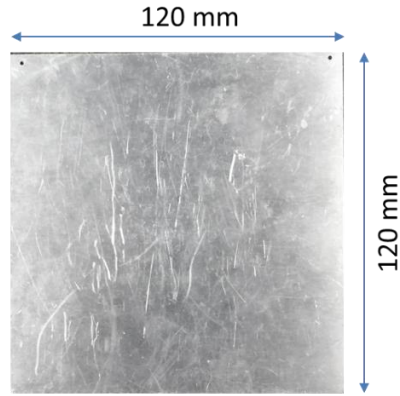
(a)
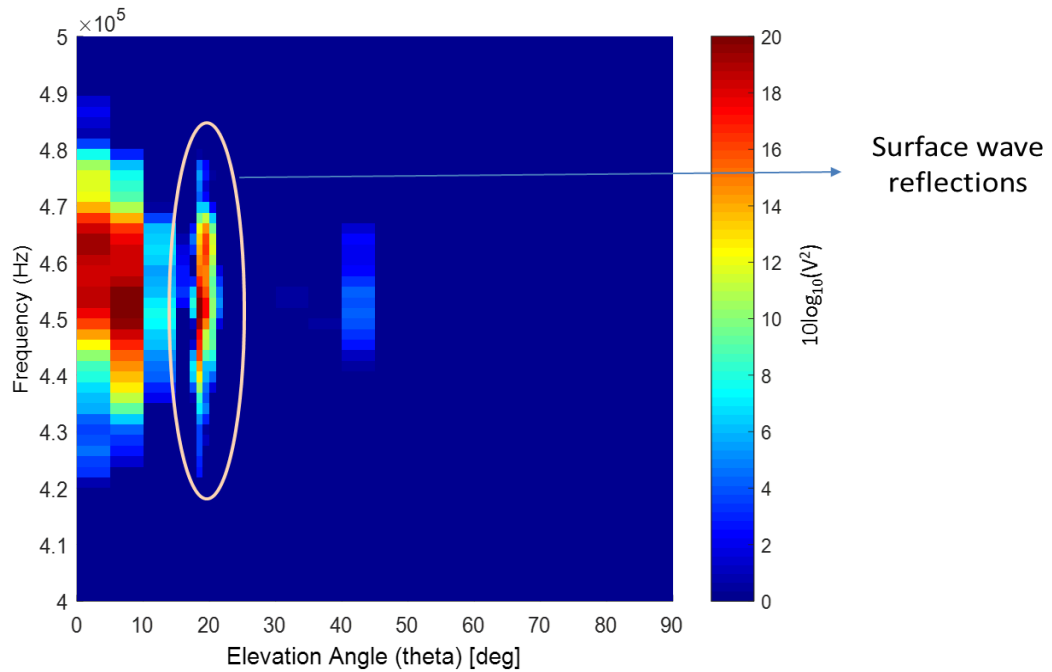
(b)

Figure 23: a) Picture of control tag; b) Scattered pressure amplitude (in logarithmic scale) observed at the SONAR for varying elevation angles θ, azimuth angle $\Phi = 0°$ at the SONAR beam band for the control tag at $R = 2m$

Besides the normal specular reflection seen at $\theta = 0°$, Figure 23b suggests that there is a backscattered reflection which occurs from the tag at $\theta \approx 18°$. Unlike the Bragg backscatter, this backscatter data does not show any variance with or dependence on frequency. This

behavior happens due to the mode conversion to a Rayleigh/Lamb surface wave which radiates in the water at this critical angle. Snell's law [24] can be used to identify the surface wave velocity in alumunim v_s that is seen at this incident angle of $\theta_i = 18°$, sound velocity in water $v_i = 1500m/s$, and a refracted critical angle in aluminum of $\theta_r = 90°$ for surface wave generation.

$$\frac{sin\theta_i}{v_i} = \frac{1}{v_s} \qquad [18]$$

Equation 18 suggests that a surface wave with velocity $v_s \approx 4900$ m/s is possible at the incidence angle of $\theta_i = 18°$. This surface wave velocity is very close to the Lamb/extensional wave velocity v_{ext} of 5000 m/s as seen in a thin aluminum rod [25]. Hence, the behavior in Figure 23b can be attributed to the Lamb waves reflecting back at the angles around $\theta \approx 18°$. To avoid any interference with data collection, this means that the AcoustiCode tags have to be designed for a Bragg angle $\theta_{bragg} \geq 25°$. Taking a limited range $25° \leq \theta_{bragg} \leq 75°$, this gives a corresponding periodicity range for the AcoustiCode tags as $3.9\ mm \leq \Lambda \leq 1.7\ mm$. Keeping this range of periodicity in mind, different AcoustiCode tags were designed and tested at different orientations of incoming beam.

5.2 Bragg Backscatter testing at 0° Azimuth Angle

A ridge tag with periodicity $\Lambda = 3$mm (shown in Figure 24a) was tested at varying distances R from the SONAR to determine the ideal distance from SONAR to tag. Figure 24b shows the differences in the SONAR beam falling on the tag at the different distances. At a distance of 2m the main beamwidth falls within the tag, whereas for the 3.2m and 4.3m ranges, the beam hits the edges of the tags. This can result in a portion of the beam being reflected by the edges. Figure 25 illustrates the experiment results obtained for the three cases shown in Figure 24b.
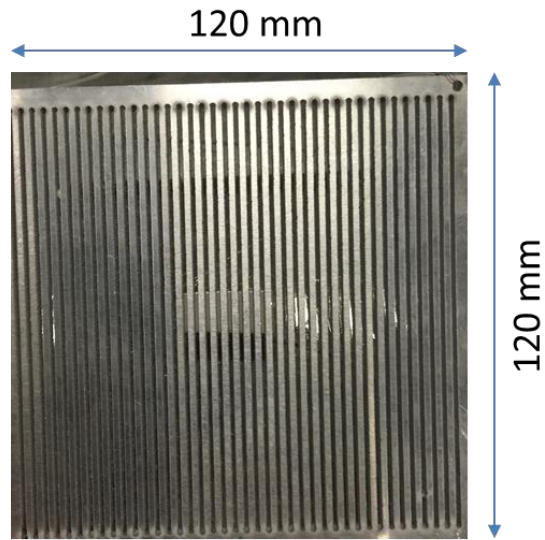
(a)
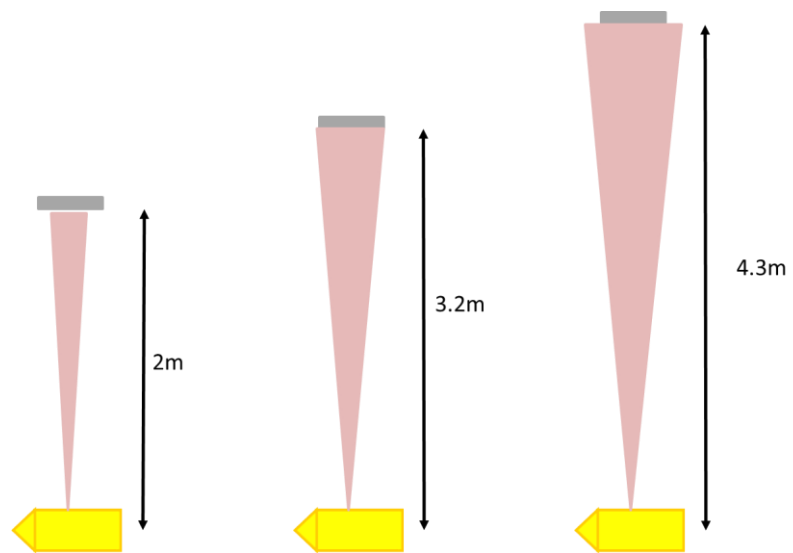
(b)

Figure 24: a) Ridge tag with periodicity Λ = 3mm; b) Schematic diagram showing ranges for test of the given tag

Figure 25: a) Scattered pressure amplitude (in logarithmic scale) observed at the SONAR for varying elevation angles θ, azimuth angle $\Phi = 0°$ at the SONAR beam band for the ridge tag with periodicity $\Lambda = 3mm$ at a) $R = 2m$; b) $R = 3.2m$; c) $R = 4.3m$ (white curve plots the theoretical 3-D Bragg scatter given in Equation 6)

The experiment results obtained for the ridge tag seem to match very well with the simulation results presented in Figure 14b. This validates the experimental existence of Bragg backscatter. Even though there isn't any significant difference in the amplitude of

the pressure backscattered in the Bragg regime between the three results, Figure 25 suggests that the 120×120mm ridge tag performs the best at a distance of 2m away from the SONAR (out of the three data points collected). Figure 25a presents the cleanest dataset since the main beamwidth always falls within the tag for all elevation angles. When the beam covers the entire tag, there is some reflection back off the edges of the tag. However, these reflections can be differentiated from the Bragg backscatter since they do not have any apparent frequency dependence i.e. they do not follow the curve represented by the theoretical result overlaid in Figure 25. Based on this result, the circular tag was also tested at a distance of $R = 2m$ from the SONAR. Figure 26a shows the circular tag which was tested; the corners have been covered with butyl rubber (acting as a sound absorber at these high frequencies) so that the SONAR beam mainly reflects from the circular area.

(a)   (b)

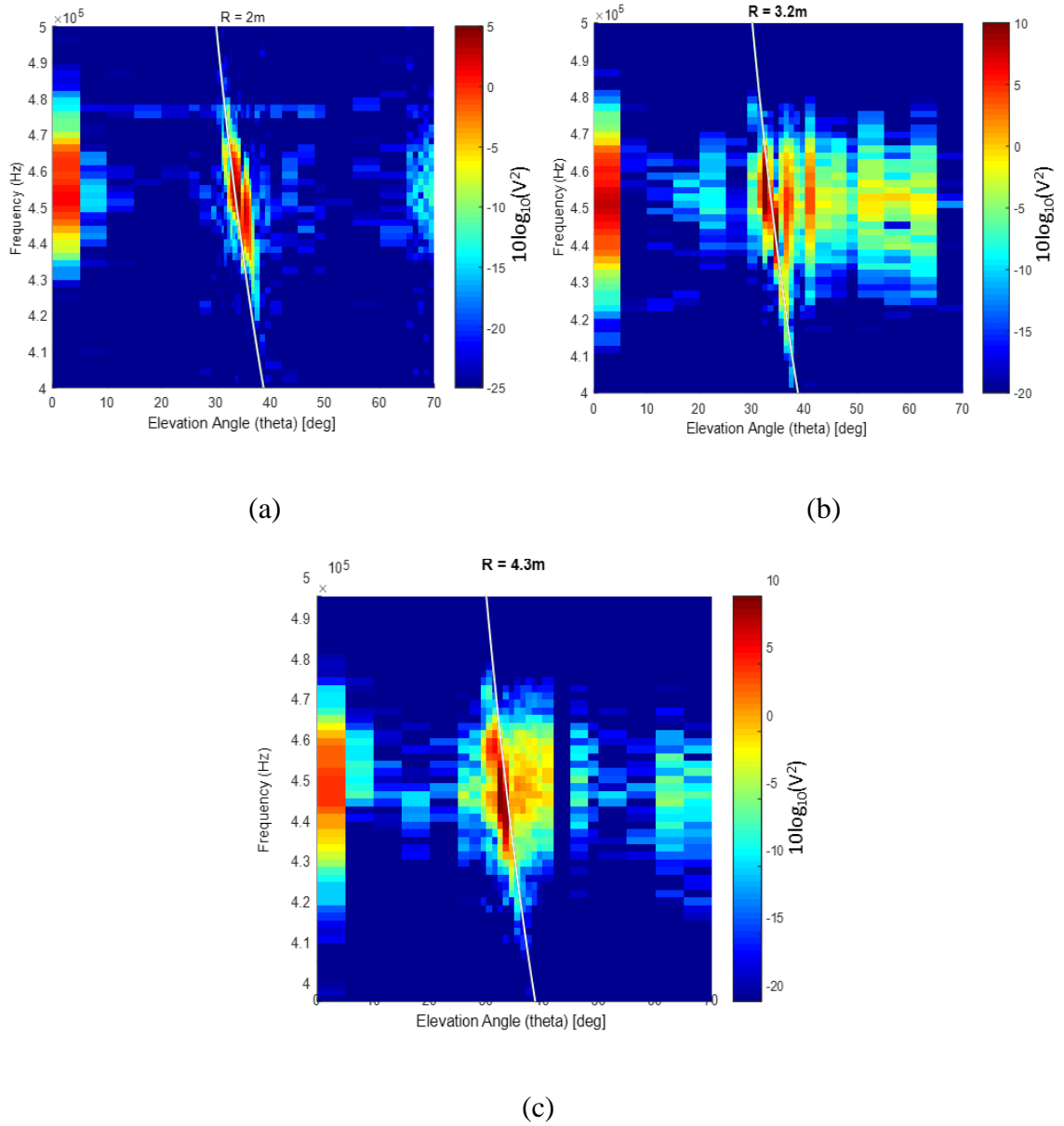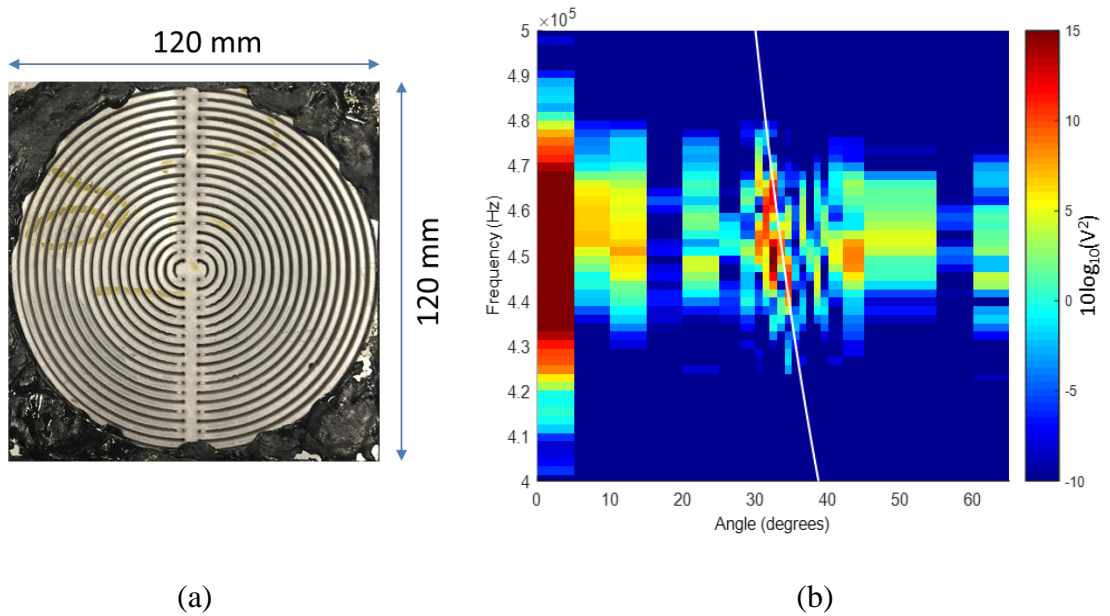Figure 26: a) Circular tag with periodicity $\Lambda = 3mm$; b) Scattered pressure amplitude (in logarithmic scale) observed at the SONAR for varying elevation angles θ, azimuth angle $\Phi = 0°$ at the SONAR beam band for the given circular tag at $R = 2m$ (white curve plots the theoretical 3-D Bragg scatter given in Equation 6)

As predicted by the simulations, the circular tag has a smaller Bragg scatter amplitude as compared to the ridge tags. This is evident in Figure 26b since the Bragg backscatter curve observed is only a few dB points higher than the background noise. The next step is to investigate the difference in the Bragg backscatter amplitudes observed for the two tag types at varying azimuth angles Φ.

5.3 Bragg Backscatter at Varying Azimuth Angle

The ridge tag with periodicity Λ = 3mm was tested at an azimuth angle Φ = 20°. The aim of the experiment was to compare the differences in the backscatter amplitude of the tag versus that of the circular tag and that of ridge tag at Φ = 0°. To vary the azimuth angle, the tag was rotated around x axis, as shown in the schematic in Figure 27a. Figure 27 compares the three cases.
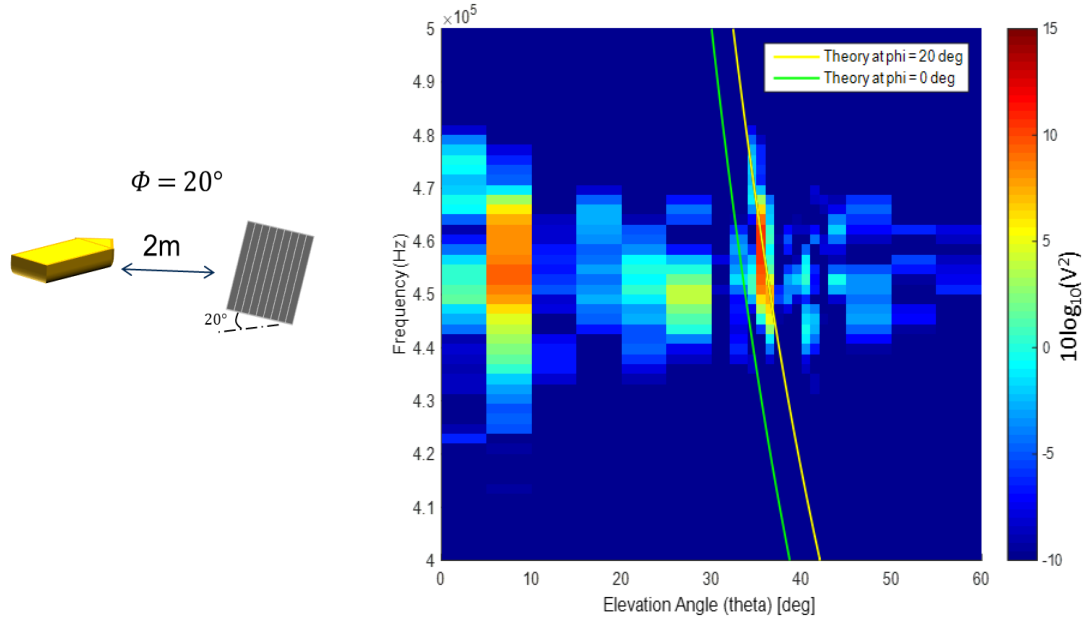
(a)
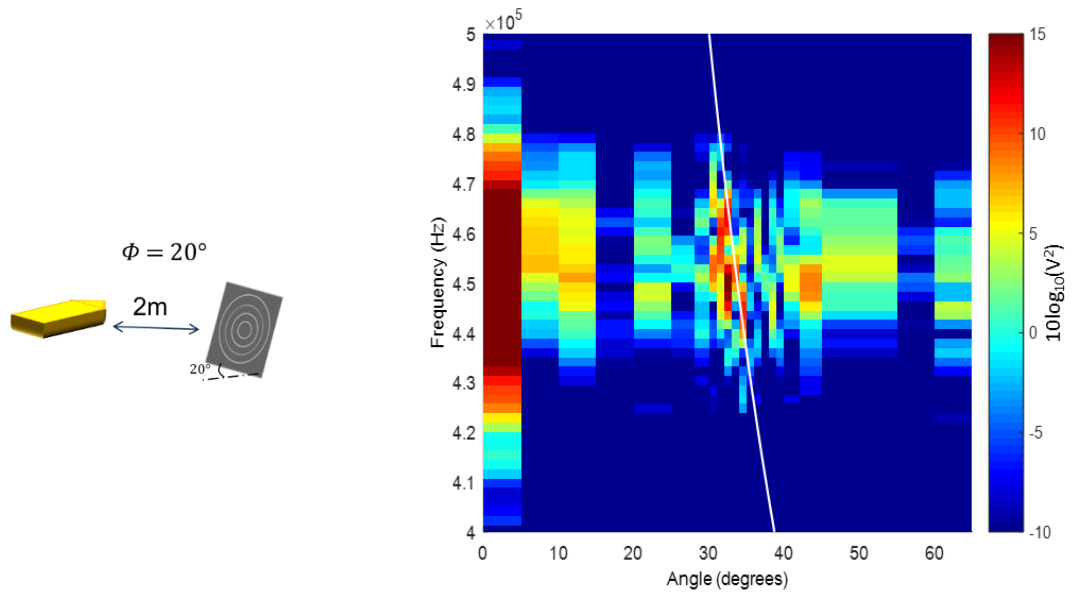
(b)

Figure 27: Scattered pressure amplitude (in logarithmic scale) observed at the SONAR for varying elevation angles θ, at the SONAR beam band at $R = 2m$ for a) ridge tag with periodicity $\Lambda = 3mm$ at azimuth angle $\Phi = 20°$; b) circular tag with $\Lambda = 3mm$ at $\Phi = 20°$; c) ridge tag with $\Lambda = 3mm$ at $\Phi = 0°$ (all plots on the same color scale); (theoretical curves plot the 3-D Bragg scatter given in Equation 6)

$\Phi = 0°$
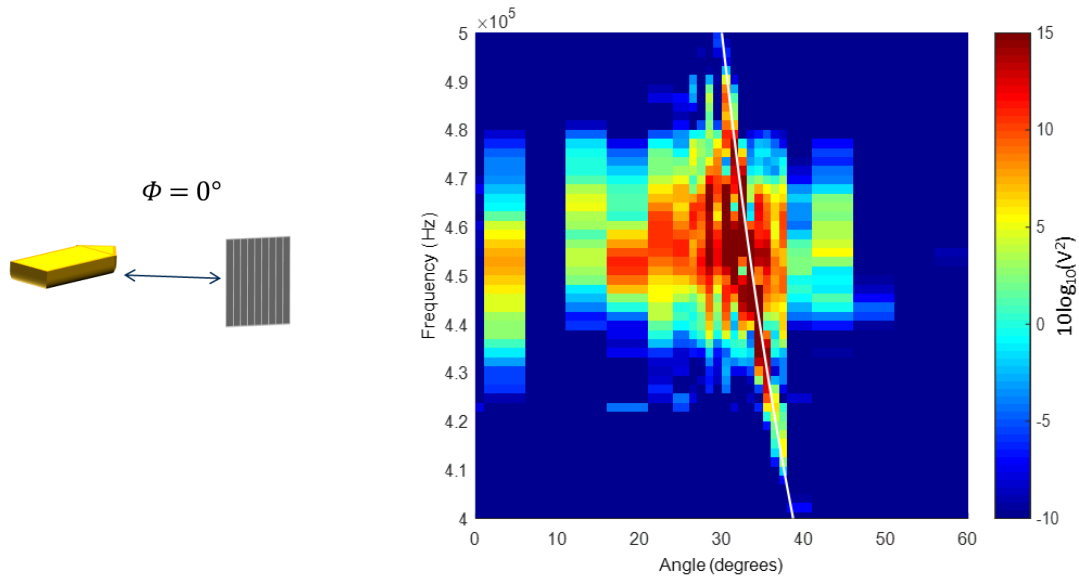
(c)

Figure 27 continued

Figure 27a validates the result shown in Figure 17a, where in a shift in Bragg regime is observed with the change in Φ; the experimental result matches the theoretical shift in Bragg regime for $\Phi = 20°$. The Bragg backscatter amplitudes also follow the simulation results, where in the ridge tag at $\Phi = 0°$ provides the highest reflection, followed by the circular tag, followed by ridge tag at $\Phi = 20°$ with the least reflection. The pressure amplitude decreases with increasing azimuth angle Φ.

However, even at this small reflection, the Bragg curve can be identified. This result provides a proof of concept for the AcoustiCode tag navigation method described in Figure 19. With a better spatial resolution and a broader frequency band of SONAR, a higher definition of SONAR image can be produced for increasing azimuth angles (where in the backscattered pressure is expected to decrease furthermore).

49

A multiple periodicity tag is also tested to understand the possibility of encoding further bits of information using the tag.

5.4 Multiple Periodicities Tag

A multiple periodicity ridge tag (Λ = 2.0, 2.2, 2.5, 3.0 mm) was designed with 4 different 120×120 mm ridge tags put together, as shown in Figure 28. Since this tag is larger than the other tags tested earlier, it was placed at a distance of $R = 4m$ from the SONAR to allow the entire tag to be ensonified by the SONAR beam. Figure 29 shows the two experiment trials conducted along with the beam geometries incident on the tag in the two cases.
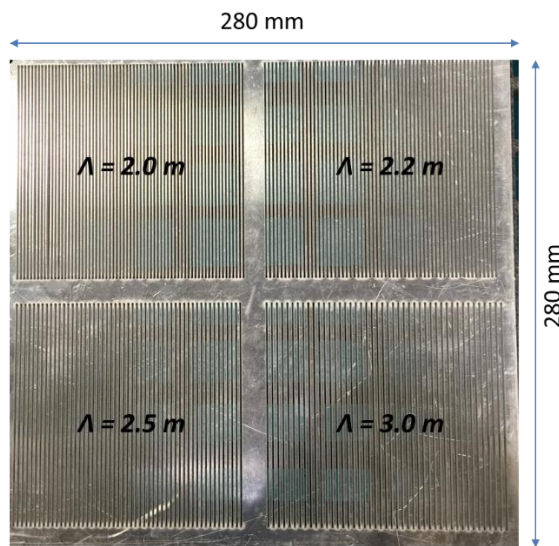
Figure 28: Multiple periodicity ridge tag with Λ = 2.0, 2.2, 2.5, 3.0 mm

Figure 29 validates the multiple periodicity tag simulation shown in Figure 20, and provides a proof of concept for the multiple tag navigation system proposed by Figure 21. This suggests that for a tag with four different periodicities as given here, up to 4-bit information can be encoded. However, care must be taken that the beam covers all the periodicities in the tag. For the given SONAR-tag distance of 4m in Figure 29, the beam

didn't manage to encompass the entire tag. Hence, two trials were conducted by changing the location of incidence beam falling on the tag. In both the cases, all 4 Bragg regimes did appear. However, for Figure 29a the bottom two periodicities appear brighter, whereas in Figure 29b the top two periodicities appear brighter because a higher percentage of the beam falls on the respective periodicities.
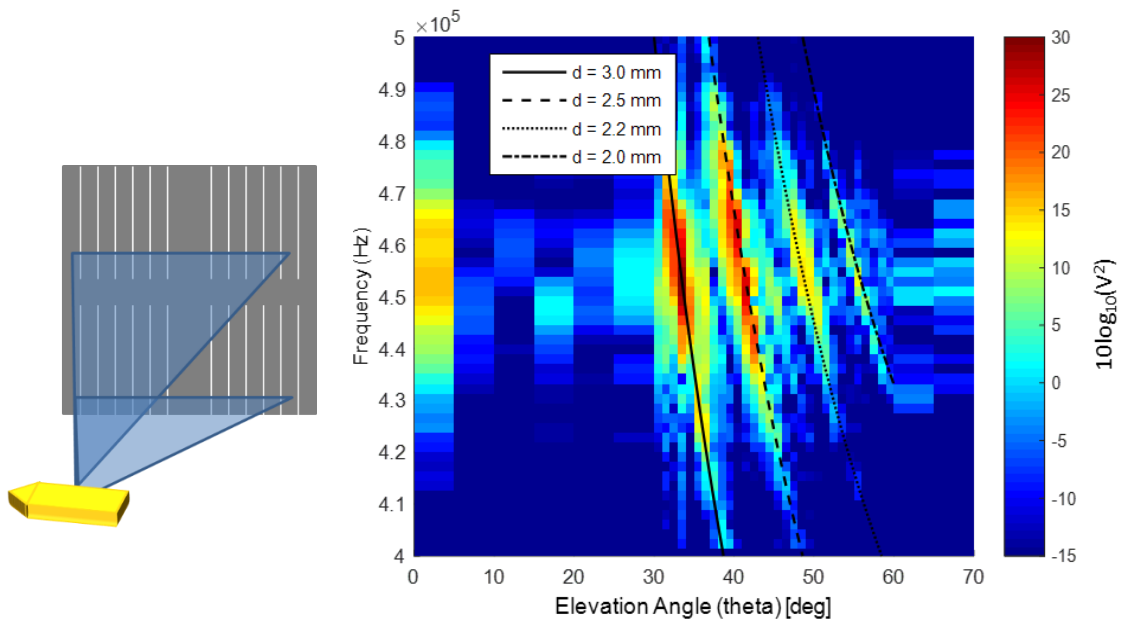
(a)

Figure 29: Scattered pressure amplitude (in logarithmic scale) observed at the SONAR for varying elevation angles θ, azimuth angle $\Phi = 0°$ at the SONAR beam band at $R = 4m$ a) Trial 1 with beam focused on bottom section of tag; b) Trial 2 with beam focused on top section of tag; (theoretical curves plot the 3-D Bragg scatter given in Equation 6)
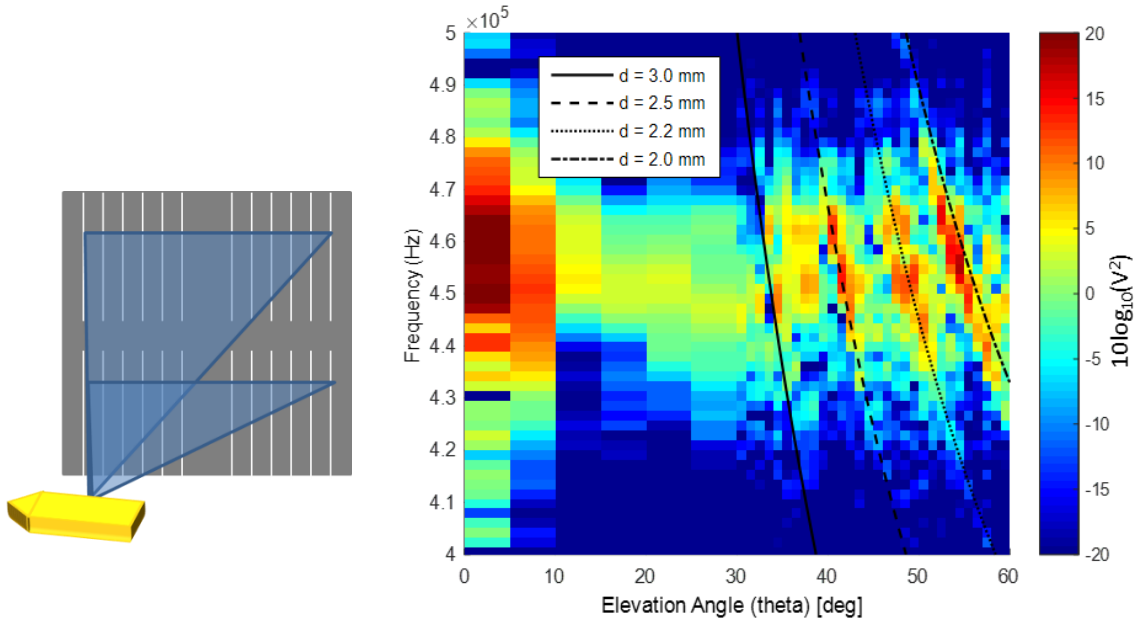
(b)

Figure 29: continued

Overall, the theoretical predictions and calculations performed by the simulation were in good agreement with the experiment results. The experiment results provide a proof of concept for a navigation system that can utilize the unique 3-D Bragg scattering exhibited by periodic AcoustiCode ridge tags (i.e. as a function of both elevation angles θ, azimuth angle Φ) upon incidence from a broadband SONAR beam. Furthermore, multiple periodicities were shown to be able to add extra bits of information to the tag.

CHAPTER VI

CONCLUSION

This work developed a model to predict the 3-D scattering from a periodic 2-D surface when ensonified by a SONAR beam. Different types of periodic tags were studied, and an AcoustiCode tag navigation system was proposed by taking advantage of the unique 3-D Bragg backscatter maps observed for ridge tags. Given a broadband frequency, the movement trajectory of the SONAR can be obtained by comparing the pressure return signal at the SONAR against the known Bragg regime of a given AcoustiCode tag. Multiple periodicities were added to the tag to increase the bits of information that can be encoded to the SONAR receiver. Underwater tank experiments were in good agreement with theoretical predictions of the model.

The results of this work provided a proof of concept to suggest that AcoustiCode tags can be utilized for applications requiring underwater navigation or encoding of information. However, further work may be required to refine the tag navigation system. Development of more complex tag designs (with help of the simulation model to predict the tag response), use of broader band sonars, and conducting at-sea experiments, can help guide future growth of this passive acoustic tag system.

APPENDIX A

CHOOSING SAMPLING PERIOD FOR BEAM SIMULATION

This Appendix describes the method used for choosing a suitable sampling period for simulating the beam used for model. For a sampling period of δk_y which equals $sin\left(\delta\frac{\omega}{c}\Delta\right) \approx \delta\frac{\omega}{c}\Delta$, the corresponding sampling period in y-axis δy (or T) can be given as:

$$\delta y = T = \frac{2\pi}{\delta k_y} = \frac{2\pi c}{\omega\delta\Delta} \qquad [19]$$

(a) (b)
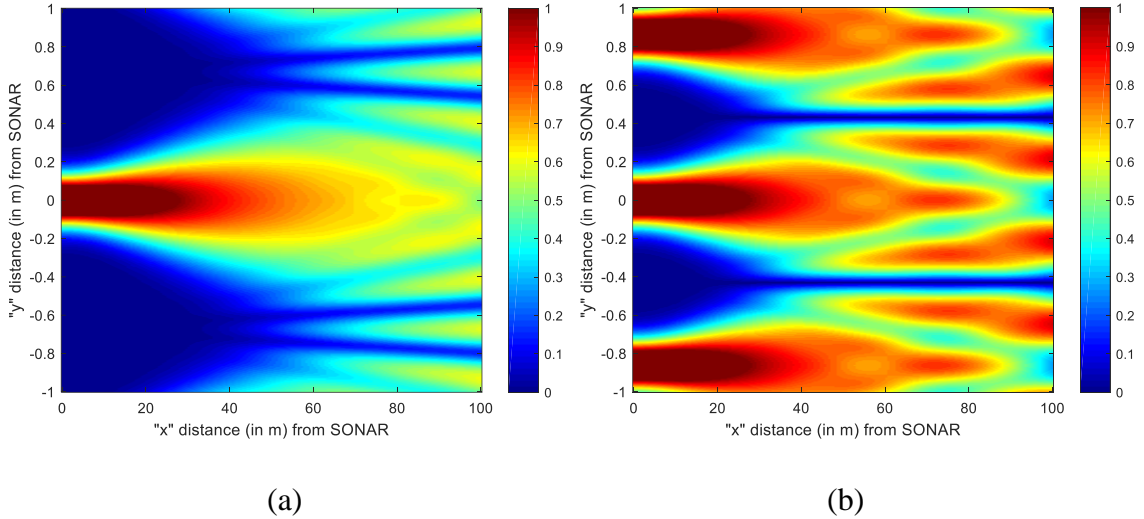
Figure 30: SONAR beam pressure amplitude (in P/P_0) in the x-y plane with a) $\delta\Delta = 0.14°$, b) $\delta\Delta = 0.22°$

For Figure 30a, 30b, T is 1.3m, 0.83m respectively, which suggests that the next beam is spaced at that distance from the current beam in y-axis. Using geometry of the beams, the intersection point R_{max} between the two beams can determined as:

54

$$R_{max} = \frac{T}{2tan\left(\frac{\Delta}{2}\right)} = \frac{\pi c}{\omega(\delta\Delta)tan\left(\frac{\Delta}{2}\right)} \qquad [20]$$

Equation 20 predicts the relationship between the sampling period of the beamwidth, and the maximum distance until which the tag can be simulated. This results in R_{max} values of 37m and 24 m for Figure 30a, 30b respectively. Hence, to increase the range of R_{max} in the simulation, $\delta\Delta$ should be small enough, as described in Equation 20.

APPENDIX B

SIMULATION FRAMEWORK PROCESS FLOW

The following flowchart shows the simulation model process and the interactions of the different components/functions of the model.

Create Tag
- Output tag geometry matrix as a binary periodicity density function with 1's and 0's
- Three types of tag options - 'ridge', 'grid', 'circular'

Simulate Beam
- Simulate beam as a Gaussian amplitude distribution for angles within the beamwidth
- Output discrete wave vectors and their corresponding amplitudes

Spatial FFT
- Carry out spatial Fourier Transform of the periodic tag geometry matrix
- Output direction of periodicities G and their corresponding amplitudes n_G (above a chosen threshold)

Frequency Bandwidth
- Gaussian amplitude distribution for frequencies within the bandwidth
- Output discrete frequencies and their corresponding amplitudes

Beam from SCS to TCS
- Input incoming beam angles (both elevation and azimuth)
- Rotate beam vectors from SONAR Coordinate System to Tag Coordinate System

Calculate F
- Loop over each discrete wave within the beam
- Loop over each discrete frequency within the band
  - Calculate the scattering amplitude F using Equation 12

Calculate P
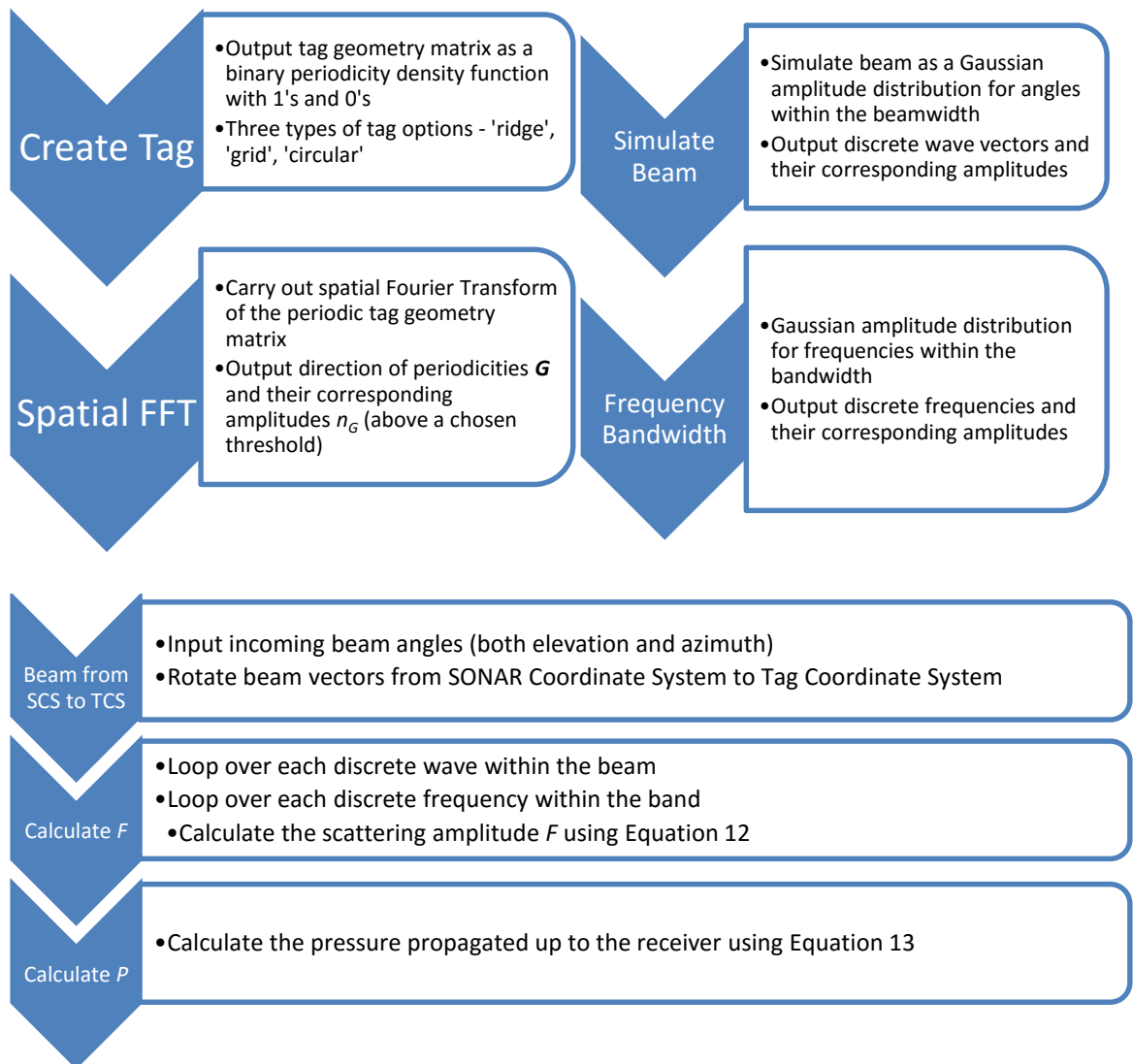- Calculate the pressure propagated up to the receiver using Equation 13

Figure 31: Flowchart showing the simulation model process flow

APPENDIX C

MODIFIED DATA ACQUISITION

The raw SONAR return signal data is obtained from the Starfish 450 Top Box (setup schematic given in [12]) by connecting to a NI USB 5133 digitizer as shown in Figure 32. The SONAR outputs a trigger signal of upto 150V pk-pk, and a return signal is measured (in the range of 10-20mV pk-pk). The NI digitizer can only handle a signal input with a maximum up to 30V. Hence, a voltage protection circuit is needed to clip the initial trigger signal obtained from the SONAR. Figure 33 shows the step-down circuit used as an intermediate to connect between the Starfish Top Box and the NI digitizer.
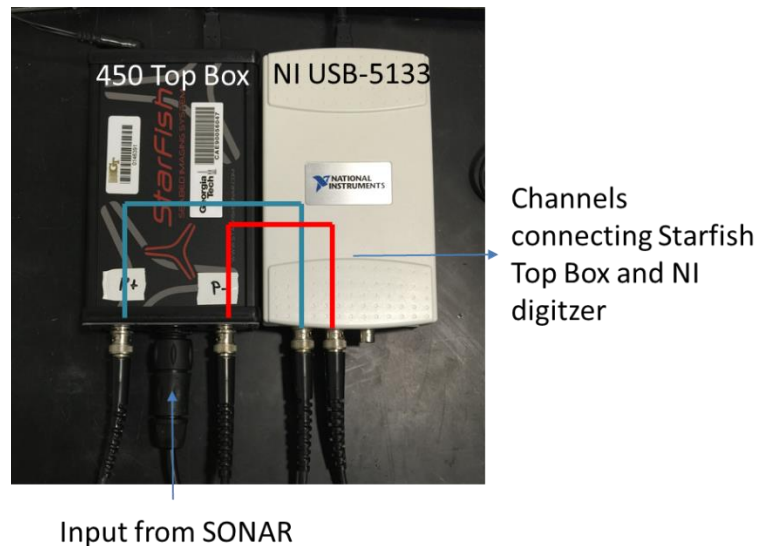
Figure 32: Picture of Starfish 450 Top Box in connection with the NI USB-5133 digitizer
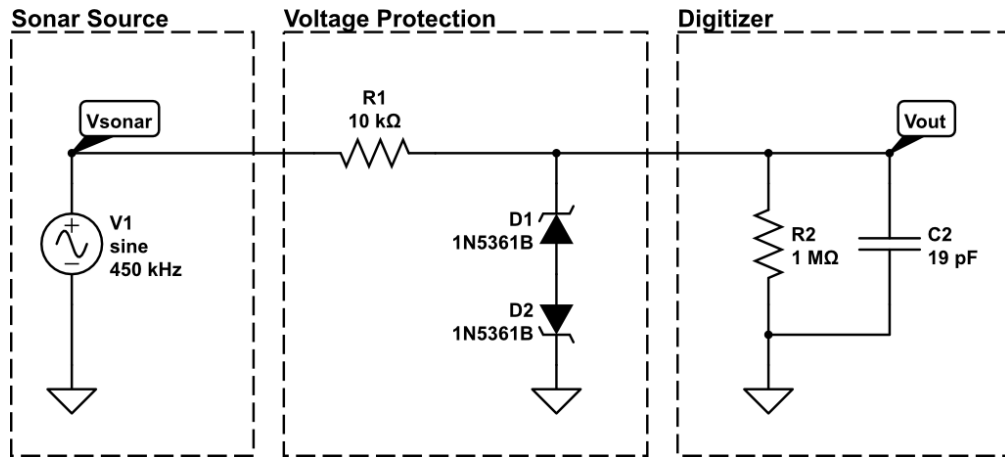
Figure 33: Schematic of step-down circuit connection between the Starfish 450 Top Box and the NI USB-5133 digitizer

The voltage protection circuit shown in Figure 33 uses a 10kΩ resistor along with 2 Zener diodes. The 10kΩ resistor steps down the output voltage in the linear region should by 82.7% of the input. The Zener diodes shunt the current to ground if the voltage exceeds 28V, which causes the input voltage to remain below 28V.

REFERENCES

[1] Jun-Hong, C., Jiejun, K., Gerla, M., Shengli, Z., "The challenges of building mobile underwater wireless networks for aquatic applications," in *Network, IEEE*, vol.20, no.3, pp.12-18, 2006.

[2] Jiang, S. and Georgakopoulos, S., "Electromagnetic wave propagation into fresh water," in *Journal of Electromagnetic Analysis and Applications*,*3*(07), pp.261. 2011.

[3] Leonard, J. J., Bennett, A. A., Smith, C. M., & Feder, H., "Autonomous underwater vehicle navigation," in *IEEE ICRA Workshop on Navigation of Outdoor Autonomous Vehicles,* Leuven, Belgium*,* May 1998.

[4] Vickery, K., "Acoustic positioning systems. A practical overview of current systems," in *Autonomous Underwater Vehicles, 1998. AUV'98. Proceedings of the 1998 Workshop on*, pp. 5-17. IEEE, 1998.

[5] Stojanovic, M., "Underwater acoustic communications," in *Electro/95 International. Professional Program Proceedings*, pp.435-440, 1995.

[6] Stojanovic, M., Catipovic, J. and Proakis, J.G., "Adaptive multichannel combining and equalization for underwater acoustic communications," in *The Journal of the Acoustical Society of America*, *94*(3), pp.1621-1631. 1993.

[7] Domingo, M.C., "An overview of the internet of underwater things," in .*Journal of Network and Computer Applications*, *35*(6), pp.1879-1890. 2012.

[8] Watkins, W. A., Daher, M. A., Fristrup, K. M., Howald, T. J., Sciara, D., & Notarbartolo, G., "Sperm whales tagged with transponders and tracked underwater by SONAR," in *Marine mammal science*, *9*(1), pp. 55-67. 1993.

[9]   Dijk, Esko Olavi, and Cornelis Hermanus Van Berkel., "Low Cost Acoustic Responder Location System." Koninklijke Philips Electronics N.V., assignee. Patent US 20080151692 A1. 26 June 2008.

[10] Dudek, G., Giguere, P., Sattar, J., "Sensor-based behavior control for an autonomous underwater vehicle." in *Experimental Robotics.* pp. 267-276. Springer Berlin Heidelberg. 2008.

[11] de Jong, C.D., Lachapelle, G., Skone, S. and Elema, I.A., "Multibeam SONAR theory of operation" (pp. 5-1 - 5-15). Delft, the Netherlands: Delft University Press, 2002.

[12] Blueprint Subsea., "StarFish 452F Advanced Towed Sidescan System," Web. <http://www.blueprintsubsea.com/pages/product.php?PN=BP00184>.

[13] Flemming, B.W., "Side-scan SONAR: a practical guide," in *The international hydrographic review*, *53*(1). 2015.

[14] Henriques, V. and Mendes, B., "Recommended Operating Guidelines (ROG) for sidescan SONARs," in *MeshAtlantic*, 2013.

[15] Bragg, W., "The diffraction of short electromagnetic waves by a crystal," in *Proceedings of the Cambridge Philosophical Society*, pp. 43-57. 1913.

[16] Quentin, G., De Billy, M., Tenoudji, F.C., Doucet, J. and Jungman, A., "Experimental results on the scattering of ultrasound by randomly or periodically rough surfaces in the frequency range 2 to 25 MHz," in *1975 Ultrasonics Symposium.* pp. 102-106. IEEE. 1975.

[17] Herbison, S., "Ultrasonic Diffraction Effects on Periodic Surfaces," Ph.D Thesis, Georgia Institute of Technology, 2011.

[18] de Billy, M., Cohen-Tenoudji, F., Jungman, A., & Quentin, G. J., "The possibility of assigning a signature to rough surfaces using ultrasonic backscattering diagrams," in *IEEE Transactions on Sonics Ultrasonics*, *23*, pp. 356-363. 1976.

[19]   Blessing, G.V., Eitzen, D.G., Ryan, H.M. and Slotwinski, J.A., "Surface micrometrology using ultrasound," in *Ultrasonics Symposium, 1990. Proceedings., IEEE 1990*. pp. 1047-1052. IEEE. December 1990.

[20]   Kersemans, M., Van Paepegem, W., Van Den Abeele, K., Pyl, L., Zastavnik, F., Sol, H. and Degrieck, J., "Ultrasonic Characterizaion of Subsurface 2D Corrugation," in *Journal of Nondestructive Evaluation*, *33*(3), pp.438-442. 2014.

[21]   Jungman, A., Adler, L. and Quentin, G., "Ultrasonic anomalies in the spectrum of acoustic waves diffracted by periodic interfaces," in *Journal of Applied Physics*, *53*(7), pp.4673-4680, 1982.

[22]   Mampaert, K. and Leroy, O., "Reflection and transmission of normally incident ultrasonic waves on periodic solid–liquid interfaces," in *The Journal of the Acoustical Society of America*, *83*(4), pp.1390-1398. 1988.

[23]   Kittel, C., "Wave Diffraction and the Reciprocal Lattice," in *Introduction to Solid State Physics*, Wiley, pp.27-32, 2005.

[24]   Drury, J., "Ultrasonics. Part 3. Refraction and mode conversion," in *Insight*, *47*(1), pp.44-46, 2005.

[25]   Blattenberger, K., "Velocity of sound in Various Media," RF Cafe. Web. http://www.rfcafe.com/references/general/velocity-sound-media.htm

[26]   Soon, T.J., "QR code," in *Synthesis Journal*, *2008*, pp.59-78. 2008.

[27]   Tritech, "starfish-452f-high-frequency-side-scan-soanr.pdf," Web. <http://www.tritech.co.uk/media/products/starfish-452f-high-frequency-side-scan-soanr.pdf>